Published in final edited form as:
Nature. 2017 June 21; 546(7659): 510–513. doi:10.1038/nature22388.

A Massive Dead Disk Galaxy in the Young Universe

Sune Toft[1], **Johannes Zabl**[1,2], **Johan Richard**[3], **Anna Gallazzi**[4], **Stefano Zibetti**[4], **Moire Prescott**[5], **Claudio Grillo**[1,6], **Allison W.S. Man**[7], **Nicholas Y. Lee**[1], **Carlos Gómez-Guijarro**[1], **Mikkel Stockmann**[1], **Georgios Magdis**[1,8], and **Charles L. Steinhardt**[1]

[1]Dark Cosmology Centre, Niels Bohr Institute, University of Copenhagen, Juliane Maries Vej 32, København Ø, 2100, Denmark

[2]IRAP, Institut de Recherche en Astrophysique et Planétologie, CNRS, 9, avenue du Colonel Roche, F-31400 Toulouse, France/Université de Toulouse, UPS-OMP, Toulouse, France

[3]Centre de Recherche Astrophysique de Lyon, Observatoire de Lyon, Université Lyon 1, 9 Avenue Charles André, 69561 Saint Genis Laval Cedex, France

[4]Istituto Nazionale di Astrofisica–Osservatorio Astrofisico di Arcetri, Largo Enrico Fermi 5, 50125 Firenze, Italy

[5]Department of Astronomy, New Mexico State University, 1320 Frenger Mall, Las Cruces, NM 88003-8001, USA

[6]Dipartimento di Fisica, Universitá degli Studi di Milano, via Celoria 16, I-20133 Milano, Italy

[7]European Southern Observatory, Karl-Schwarzschild-Straße 2, 85748 Garching bei München, Germany

[8]Institute for Astronomy, Astrophysics, Space Applications and Remote Sensing, National Observatory of Athens, GR-15236 Athens, Greece

Abstract

At z=2, when the Universe was just 3 Gyr old, half of the most massive galaxies were extremely compact and had already exhausted their fuel for star formation1–4. It is believed that they were formed in intense nuclear starbursts and that they ultimately grew into the most massive local elliptical galaxies seen today, through mergers with minor companions5,6, but validating this

Correspondence and requests for materials should be addressed to S.T. (sune@dark-cosmology.dk).

Author Contributions

S.T. conceived the study, was principle investigator of the XSHOOTER program, performed the Galfit analysis and produced Figures 2, 3, 4, Extended Data Figure 3, 4 and 6. ST and JZ wrote the paper. JZ reduced the XSHOOTER data, performed the pPXF analysis and lensing model systematic error analysis. JZ also produced Figure 1 and Extended Data Figures 5 and 7. AG performed the stellar population synthesis modeling of the spectrum+photometry. SZ performed the emission line analysis, produced the resolved stellar population maps and Extended Data Figure 2. JR performed the lensing analysis, and source plane reconstruction. MP performed the MCMC dynamical modeling and produced Extended data Figure 8. CG produced the color composite HST images in Figure 1 and Extended Data Figure 1. AM performed the Galfit MCMC analysis. GM derived the SFR limit from the MIPS data. All authors discussed the results and commented on the manuscript.

Author Information

Reprints and permissions information is available at www.nature.com/reprints.

The authors declare no competing financial interests.

Europe PMC Funders Author Manuscripts

scenario requires higher resolution observations of their centers than currently possible, even from space. Magnification due to gravitational lensing offers a unique opportunity to resolve their inner regions, as demonstrated in a recent study of a z=2.6 compact spheroidal galaxy which revealed a bulge, rotating at velocities comparable to the fastest rotating local ellipticals7. Following the same approach, here we map the stellar populations and kinematics of a lensed z=2.1478 compact galaxy, which surprisingly turn out to be a fast spinning, rotationally supported disk galaxy. Rather than in a merger-driven nuclear starburst8, its stars must thus have formed in a disk, likely fed by streams of cold gas, which were able to penetrate the hot halo gas until they were cut off by shock heating from the dark matter halo9. This result unambiguously confirm indications from a growing body of indirect evidence10–13 that the first galaxies to cease star formation must go through major changes not just in their structure, but also in their kinematics to evolve into present day ellipticals.

We obtained deep spectroscopy with VLT/XSHOOTER a compact quiescent galaxy (cQG) that is gravitationally lensed by the z=0.588 cluster of galaxies MACS2129-074115 (Extended data Figure 1), and as a consequence appears 4.6 ± 0.2 times brighter and extends over 3" on the sky.

In Figure 1, we show the position of the XSHOOTER slit on an HST color-composite image, and on the reconstructed source plane. The galaxy is stretched along its major axis and we derive a spatially resolved spectrum typical of quiescent z~2 post starburst galaxies, with a strong Balmer break and a number of strong absorption features. We fit a spectroscopic redshift of z = 2.1478 ± 0.0006 and constrain the stellar populations through modeling of the rest frame UV-to-optical spectrum, absorption line indices, and spatially integrated rest frame UV-to-NIR colors derived from 16 band HST/IRAC photometry. The best-fit spectrum reveals a massive, old, post starburst galaxy consistent with negligible ongoing star formation, and at most solar metallicity $\left(\log\left(M_*/M_\odot\right) = 11.15^{+0.23}_{-0.23}\right.$, $\log(\mathrm{age/yr}) = 8.97^{+0.26}_{-0.25}$, $A_i = 0.6^{+\mathbf{0.9}}_{-\mathbf{0.6}}$ mag., $\left.\log\left(Z/Z_\odot\right) = -0.56^{+0.55}_{-0.55}\right)$ (Extended Data Table 1). We derive a velocity dispersion of **σ**=329±73 km/s from absorption lines in the spatially integrated spectrum (Figure 1) using a Penalized Pixel-Fitting method (pPXF)16 with the best fitting SED model as a template.

Interestingly, the absorption lines are tilted in the 2D spectrum. We extract individual rows that represent ~0.4 kpc bins along the major axis on the source plane. The central 11 rows have sufficient S/N to reliably detect absorption lines. We fit each row with the same pPXF implementation used for the spatially integrated spectrum to derive velocity shifts and dispersions as a function of distance from the center of the galaxy. There is a clear symmetric velocity gradient as expected for a rotating disk (Figure 2).

The observed rotational velocity reaches a maximum of $\langle|V_{max,obs}(1'')|\rangle = 341 \pm 115$ km/s (weighted mean in the two outer bins), showing unambiguously, and independent of model assumptions, that the galaxy has a higher degree of rotational support $V_{max,obs}/\sigma > 1.03 \pm 0.42$ than observed previously in any quenched galaxy. This is a conservative lower bound, as corrections for the effects of inclination, alignment of the slit, and unresolved rotation will all drive the ratio up.

We take these into account, as well as the effect of gravitational lensing, by performing a full MCMC dynamical modeling analysis. We find the velocity shifts to be well represented by the rotation curve of a thin, circular, rotating disk with a maximum rotational velocity of $V_{max} = 532^{+67}_{-49}$ km/s at $r_{max} = 0.5^{+0.8}_{-0.3}$ kpc. This implies a dynamical mass within r_e (total) of $\log\left(M_{dyn}/M_{\odot}\right) = 11.0^{+0.1}_{-0.1}\left(11.3^{+0.1}_{-0.1}\right)$. We model the observed dispersions by taking into account the effect of PSF smearing $\sigma^2_{obs}(r) = \sigma^2_{int} + \sigma^2_{sm}(r)$. This is particularly relevant in the central regions where the steep gradient of rotational velocity translates into artificially high apparent velocity dispersions.

We find that $\sigma_{obs}(r)$ is well represented by velocity smearing (σ_{sm}) alone, but can also accommodate a small intrinsic constant dispersion $\left(\sigma_{int} = 59^{+57}_{-44}\,\mathrm{km/s}\right)$.

In the central bin, σ_{obs} is ~0.5 sigma above the modeling predictions, leaving room for enhanced central dispersion; however as there is no indication of a bulge in the stellar mass map (Figure 3), it is unlikely to be very prominent. From the dynamical modeling we conclude that that the galaxy is a rotation-dominated disk with $V_{max}/\sigma_{int} > 3.3$ (97.5% confidence).

We detect weak, centrally concentrated nebular emission lines $[OIII]_{5007}$, $HeII_{5411}$, $H\alpha_{6563}$, and $[NII]_{6583}$. The (extinction corrected) Hα flux corresponds to SFR<1.1 $M_{\odot}$/yr[17], an upper bound since the line ratios indicate an AGN or LINER as the dominant ionizing source[18], consistent with what is found in local post-starburst galaxies[19]. The emission lines are redshifted by $v_{sys,em}$= 236 km/s with respect to the absorption lines, possibly due to AGN outflows (see Extended Data Figure 2 and Extended data Table 1).

Using our well constrained lens model and multi-band HST imaging, we reconstruct the galaxy on the source plane and derive spatially resolved maps of median-likelihood estimates of stellar population parameters (Figure 3). The projected mass distribution is smooth, ruling out the possibility of a close major merger causing the velocity gradient. The three other maps show indications of radial gradients, with the galaxy center having ~2 dex lower specific star formation rate (sSFR), ~0.2 dex older stellar populations, and ~0.6 mag higher extinction than the outer regions (see Extended Data Figure 3). Note however that the sSFR is consistent with zero everywhere (see error map). The quiescent nature of MACS2129-1 is further supported from its non-detection in deep Spitzer/MIPS 24μm observations, corresponding to a lensing corrected 3σ upper limit of SFR<5 $M_{\odot}$/yr.

We fit the 2D surface brightness distribution of the galaxy on the source plane. Figure 4 shows the reconstructed F160W image, the best fitting Sersic model (circularized effective radius $r_e = 1.73^{+0.34}_{-0.27}$ kpc, Sersic index $n = 1.01^{+0.12}_{-0.06}$, axis ratio $a/b = 0.59^{+0.03}_{-0.09}$, and the residual (image - model), which shows visual hints of spiral arm structure. Also shown are 1D profiles of the best fitting model, the F160W light distribution and the projected stellar mass distribution estimated from the spatially resolved SED fits. The galaxy is resolved on scales of ~250 pc, allowing accurate constraints on its inner profile to ~1/5 r_e. The light and mass profiles are well represented by an exponential disk law (n=1) out to 5 kpc (~3r_e), as

Europe PMC Funders Author Manuscripts

expected if the galaxy is a rotation-dominated disk. The outer regions ($r>3r_e$) have excess low surface brightness light, which is not associated with significant stellar mass.

MACS2129-1 presents a range of features typical of z>2 cQGs: It falls on the stellar mass-size relation for quiescent galaxies2, it has a post starburst spectrum with evolved stellar populations, a SFR more than 100 times below the z=2 SFR-M_* relation20, and $M_{dyn}/M_* = 1.55 \pm 0.40$ (within r_e), similar to what is found in other z=2 quiescent galaxies3, 4, 13. However, the increased sensitivity and resolution provided by gravitational lensing reveal underlying detailed kinematic properties and structure that are typical of late type galaxies. The V/σ is >3 times larger than in the fastest rotating local ellipticals21, but is similar to what is found in local spiral galaxies22 (see Extended Data Figure 4).

The only other kinematic study of the inner regions of lensed z>2 cQG (RG1M0150)7 revealed a dispersion dominated (V/σ=0.7±0.2) proto-bulge (n=3.5±0.9), as expected if it formed in a major merger induced nuclear starburst8.

In sharp contrast, MACS2129-1 shows no evidence of a bulge, and must have formed through other processes.

Rather than in a merger, its stars formed rapidly in a disk until quenching at z~3, which, based on the sSFR/age profiles, proceeded inside-out over a timescale of ~300Myr. Simulations show that collisions of cold gas streams with the inner disk (and with each other), can trigger isothermal shocks, behind which rapid cooling generates intense star formation7. This can lead to the build up of a central bulge that stabilizes the disk against further fragmentation, “morphologically quenching” and transforming the galaxy inside-out23. If the star formation in MACS2129-1 was fueled by cold accretion, the gas must have distributed itself throughout the disk, rather than in the center, so a different mechanism would be required in order to quench its star formation. Shock heating of the in-falling gas by the halo is a plausible scenario, given the 1013–14$M_\odot$ total halo mass indicated by its measured stellar mass24. “Halo quenching” is expected to cut off the raw material for star formation from the inside out (as the critical halo mass for shock stability in the center is smaller than at the virial radius9), but otherwise leave the structure of the galaxy untouched. This is in agreement with the dynamics and stellar population gradients observed in MACS2129-1. The AGN can also play a role in maintaining the hot gas temperature, as AGN feedback works very efficiently on dilute, shock-heated gas25.

Although the difference between MACS2129-1 and RG1M0150 is striking, both are consistent with being descendants of the highest redshift starbursts5, which show diverse properties. Their molecular gas reservoirs are in some cases distributed in compact fast spinning disks26, while in others they are centrally concentrated and dispersion dominated27. Immediately after quenching, the starbursts likely go through a transition phase where they appear as 2<z<3 dusty compact star forming galaxies (cSFGs)28 –some of which also show evidence of rapid rotation29 - before evolving into cQGs.

To evolve into a local elliptical, MACS2129-1 must undergo major structural and kinematic changes, through processes capable of both substantially increasing its size2 and transforming the spatial and orbital distribution of its stars from ordered rotation in a disk to random motion in a bulge. The same is to some extent true for RG1M0150. While already a dispersion dominated bulge, its V/sigma is much higher than similar mass local ellipticals, which are all slow rotators (V/sigma<0.2).

Simulations show that a large number of minor mergers from random directions are likely the dominant process14.

Methods

Selection of MACS2129-1

MACS J2129.4-0741 at $z = 0.588$, was first listed in the Massive Cluster Survey (MACS) catalogue15. It was observed as part of the CLASH survey30 with the HST/ACS and WFC3 in 16 broadband filters, from the near-UV to the near-IR, and with Spitzer/IRAC in the 3.6μm and 4.5μm channels. Lensing models for the cluster have been developed and presented 31,32,33. In Extended Data Figure 1 we show a composite color image constructed from the CLASH data, with the position of the XSHOOTER slit overlaid on MACS2129-1.

VLT/XSHOOTER Observation and reduction

MACS2129-1 was observed with the XSHOOTER spectrograph at ESO's VLT in four different observing blocks, executed in the nights starting on March 11, March 13, September 4, and September 13, 2011, respectively (Prog. ID: 087.B-0812(B)). Each observing block contained six integrations with 480s each, identical in all three of XSHOOTER's arms (UVB, VIS, NIR), and the slit widths were 1.0”, 0.9”, and 0.9” respectively. The slit was oriented along the maximum extent of the image of MACS2129-1 with a position angle of −10°, as shown in Figure 1. Photometric standard star observations of LTT7987, LTT3218, Feige110, and LTT7987 were taken during the same nights as the science observations. For each of the OBs at least one telluric star was observed at similar airmass and with the same instrumental setup as the science frames. The average seeing was ~0.5” in the J-band, estimated based on header information provided by the observatory which we calibrated based on point sources (telluric stars) to direct FWHM measurements. This seeing estimate is somewhat uncertain and we estimate an uncertainty of about 0”.1.

An analysis of this dataset has previously been published34. Here we take advantage of significant advances in data reduction and analysis techniques to re-visit the observations.

The ESO XSHOOTER pipeline (v. 2.6.0) with small modifications35, was used in the reduction. In the NIR we achieved the best reduction with a nodding reduction, which we for consistency used also for the UVB and VIS.

The offsets between the individual exposures were not ideally chosen for a nodding reduction of an object as extended as MACS2129-1. While for half of the OBs a nod throw of 3" was used, which is not ideal but acceptable, for two of the four OBs consecutive frames had very small position differences, rendering these pairs useless for a standard nodding reduction. As a solution we combined frames in these OBs in a not strictly temporal order, and rejected two frames in each. In this way we obtained for each of these two OBs one pair with a 3" and one with a 2" nod-throw. Excluding the rejected frames we had a total on source time of 2.67 hrs.

We reduced the data in pairs of two frames and corrected each of the reduced nodding pairs for the telluric transmittance36. We then corrected from air to vacuum wavelength scale and converted to the heliocentric velocity standard. The latter step is relevant, as the heliocentric velocity differs by as much as 44 km s^{-1} between the March and September frames. As the difference in the heliocentric velocity is comparable to the spectral resolution (~55 km s^{-1}), this correction is a very efficient way to minimize the impact of telluric features.

Finally, we combined all nodding pairs using a weighted mean. Further, we created re-binned versions of the 2D spectrum and extracted 1D spectra from the 2D frames within the various apertures used in the analysis.

Lensing model, and source plane reconstruction

The mass distribution of the cluster core has been modeled using the following strong lensing constraints: a z=1.363 source producing six images near the central galaxies37 and a triply imaged system at z=2.26 on the west side of the core38. These nine images were used to constrain a parametric model of the cluster, composed of a single large-scale pseudo-isothermal elliptical profile as well as sub-structure in the form of individual potentials for each galaxy in the cluster. Cluster members were selected through their HST colors and assumed to follow a scaling relation with constant mass-to-light ratio M/L, except for two galaxies near the cluster cores which affect the location of the images in the z=1.363 system.

The optimization of the cluster mass distribution was done with the Lenstool software38, which uses a Monte Carlo Markov Chain to provide a best-fit model together with ~2000 model realizations sampling the posterior probability distribution of each parameter of the mass distribution, including the uncertainty in the M/L ratio of each of the cluster galaxies.

We used the best-fit model as a benchmark to perform a reconstruction of all the different waveband HST images by mapping the image plane maps onto the source plane and associating each image pixel to its respective source plane position.

To estimate the effects of lensing model uncertainties on the analysis, in Extended Data Figure 5, we show distributions and correlations between parameters that characterize the lensing model realizations. These are the mean light (F160W) weighted magnification, the direction of maximum magnification at the center of the galaxy, and the amount of magnification in this direction and the perpendicular direction. The variations of these quantities are small, e.g. the mean light weighted magnification only display mild variations over the realizations $\langle \mu \rangle_{lw} = 4.6 \pm 0.2$. Even the most extreme magnification values (4.2 and 5.6 respectively) deviate less that 20% from the median. Similar conclusions are drawn for the direction of the magnification, measured at the center of the galaxy.

Lensing model uncertainties propagate into the measurement of structural and kinematical parameters, as also demonstrated in Extended Data Figure 5. E.g., the derived galaxy axis ratio and position angle, which are used as priors in the kinematical analysis, are strongly correlated with both strength and orientation of the lensing. However, as the lensing model

Europe PMC Funders Author Manuscripts

uncertainties are small, uncertainties on structural parameters derived from Galfit are also small (see also Extended Data Figure 6).

Finally, to demonstrate the validity of the use of a constant lensing kernel for simulating the seeing in the dynamical modeling, we quantified the spatial gradients of the scalar magnification over the galaxy in Extended Data Fig. 7, both for a typical realization, and for the realizations with the highest and lowest lensing magnifications. There is some variation caused by a cluster galaxy 3.5 arcsec to the west. The impact at the position of the MACS2129-1 is however relatively small: over the full extent of the galaxy the magnification changes by about 30 %, but within the spatial bins defined by the slit and the spatial binning used for the kinematic measurement the light weighted magnification (taking into account the seeing), does not change by more than 5%.

The reason why the model magnification is so stable for MACS2129-1 is its position 1 arcmin west of the core, outside of the strong lensing region where the magnification is high and sensitive to mass substructures associated to the high density of cluster galaxies. Outside the core, the lensing magnification is dominated by the diffuse dark matter distribution of the cluster, which is well constrained by the many multiple images. A good level of precision and accuracy in the reconstruction of images far from the critical curves is a general result, which has been proven within the HST Frontier Fields initiative, through detailed comparison of blind predictions of several modelers on simulated galaxy clusters39.

Spectral Stellar Population Characterization

We constrained the global stellar mass, age, metallicity and extinction of MACS2129-1 by fitting the spatially integrated UV-NIR XSHOOTER spectrum with stellar population synthesis models, following the procedure described in Toft et al4 but adopting a different model library that better reproduces the current star formation activity.

Briefly, we employ a library of 500000 model spectra based on BC03 stellar population models convolved with random star formation histories (SFHs). We assume a Chabrier initial mass function40. The SFHs are modeled with a delayed exponential41, on top of which random bursts of star formation can occur (Library A). We also consider a star formation history library with no additional bursts (Library B). The metallicity of the models varies along with the SFH and dust is implemented as in Charlot and Fall42 We adopt a Bayesian approach in which all models in the library are compared to the observed spectrum. Details of the adopted SFH, metallicity and dust library as well as the method employed has previously been published43.

As a benchmark we fit the UVB-VIS-NIR spectrum pixel by pixel (Fit 1), but as a test of the robustness of the fit we also perform a fit to observed spectral indices:

D4000n, Hβ, $H\delta_A$, [Mg_2Fe], [MgFe]', combined with optical-NIR (CLASH) and MIR (IRAC) broadband data (Fit 2). The marginalized median-likelihood parameters are listed in Extended Data Table 1. Reassuringly, these all agree to within estimated uncertainties. The galaxy is massive, old, and within uncertainties consistent with being void of dust and star formation. The metallicity is quite uncertain, but has an upper confidence limit of approximately solar in all fits. The large uncertainties on the metallicity is reflected in the uncertainties of the other parameters compared to fits assuming a fixed metallicity3, but we choose to keep it free in the fit, as we do not have any empirical evidence for the metallicity in z=2 quenched galaxies.

In addition to fitting the global properties in the spatially integrated spectrum, we also consider a fit to a "central" ($|r|<0.5$"), and an "outer" (0.5" < $|r|$ < 1.4") extraction to look for spatial variations.

Derivation of Rotation Curve

We used pPXF (v.6.0) to determine the velocity centroid (redshift) and dispersion both for the integrated spectrum and individual spatial rows of the rectified 2D spectrum. The individual rows correspond to a spatial extent of 0.21" each.

Because the individual rows have low S/N for kinematic fitting (central row S/N =3 $Å^{-1}$ at 1.05" S/N =1 $Å^{-1}$), it is crucial to minimize the degrees of freedom and maximize the amount of information. In this sense, we derive our fiducial results based on the best-fit stellar population fit and used only low order correction polynomials (2^{nd} order additive and multiplicative over the full rest-frame range from 3750Å to 5650Å, excluding only a window from 4200Å to 4750Å (gap between J and H band) and the [OIII] λλ 4959,5007 lines. Certainly, the inclusion of the 4000Å break combined with low order correction polynomials is a potential concern for template mismatch. We quantified potential template mismatch similar to other studies3,13 through a range of test including different correction polynomials, different templates, and different wavelength ranges. The full error budget includes both statistical and systematic uncertainties.

We determined the statistical uncertainties by running pPXF on 1000 realizations of the data. These realizations were created by randomly perturbing the best-fit model obtained by pPXF using the estimated uncertainties from the pipeline's error spectrum. This method correctly accounts for the increased noise in regions of telluric emission and absorption lines, if the error spectrum is correct. In this sense, correlated noise is a potential problem, as it is not accounted for by the pipeline. The correlation is mostly removed in the re-binned spectra used for our analysis, though. However, estimated per pixel uncertainties obtained through standard error propagation from the non-binned error-spectrum is a wavelength dependent under-estimation due to correlation at the original pixel-scale. We therefore decided to scale a propagated error map to a reduced χ^2 of one. To do so we first calculated a running reduced χ^2 over 50 pixels and fitted a second order polynomial to the resulting wavelength dependent curve, making use of clipping against outliers. By dividing the formal error spectrum by this fit, we obtained the corrected error spectrum.

To assess systematic uncertainties which are primarily due to template mismatch., we performed several tests for the integrated spectrum. For this spectrum the S/N is sufficiently high (S/N = 6.4 $Å^{-1}$) so that the tests are feasible without being completely dominated by statistical uncertainties.

Europe PMC Funders Author Manuscripts

First, we assessed the impact of the choice of correction polynomials when using our fiducial best-fit stellar population template. We tested all combinations of multiplicative (m) and additive (a) correction polynomials up to 24th order each, finding a minimum and maximum dispersion of 271km/s and 361km/s, obtained for m=0/a=24 and m=7/a=7 polynomials, respectively. The median dispersion from all polynomial combinations is with 334km/s very close to the value obtained for our default correction polynomial set (m=2/ a=2). It is reassuring that our chosen set of low-order polynomials gives a typical result.

As a second test, we checked the impact of changing the wavelength range included in the fit, while keeping the low-order correction polynomials and the fiducial template. We increased the start wavelength range from 3750Å up to 4050Å in steps of 5Å. At 4050Å only Hδ and Hβ are left in the wavelength interval outside of the telluric absorption windows. Similarly, we incrementally decreased the end wavelength from 5650Å down to 4050Å, again in steps of 5Å. At 4050Å Hδ, Hβ are excluded and only higher Balmer and the Ca H+K lines are remaining. Finally, we tested excluding 1600km/s wide windows with the range of tests covering the complete included wavelength range (5Å steps). There is some indication that the more the information is dominated by Hβ, the higher the preferred dispersion is.

First, the exclusion test gives the lowest dispersion when Hβ is excluded (280 km/s). Secondly, the dispersion rises slightly with increasing the start wavelength.

The lowest dispersion value is obtained when setting the start wavelength to 3775 Å (320 km/s) and the highest dispersion values is reached for a start wavelength of 4030 Å (400 km/s). When changing the end-wavelength, the lowest velocity dispersion is reached for an end wavelength of 4085 Å (290km/s).

Such a change of the measured velocity dispersion as a function of the included wavelength interval can also be a consequence of including or excluding the 4000Å break. In a previous study, where a similar trend was observed for other galaxies, this has been attributed to template mismatch in the 4000Å break3.

Finally, we tested the impact of the template choice, with two different template sets. In one case we allowed pPXF to freely choose from BC03 SSPs with solar metallicity, and in a second case from 45 stars being a subset of Indo-US library44. The stars were chosen45 to cover the temperature space approximately uniformly between $3 \cdot 10^3$K and $42 \cdot 10^3$K and to have metallicities in the range -0.5 < [Fe/H] < 0.4. For the tests with these template sets we used correction polynomials of higher order (m =2 / a=9; about 1 order per 1000 km/s) than used for the best fit best-fit stellar population template. Higher order polynomials are needed for these template sets, e.g. to account for dust extinction. We measured velocity dispersions of 403 km/s and 386 km/s for BC03 and Indo-US, respectively.

Summing these systematic tests up, we find variations, which are of the same order as the statistical uncertainties, which is for the integrated spectrum 58 km/s. It is important to note that we had to use for the systematic tests the data itself. Therefore, the observed wavelength trend can either be due to template mismatch, may it be for lines in the 4000Å break or for Hβ, or simply due to statistical noise altering the shape of the individual lines differently. In this sense the systematic uncertainties are a conservative estimate, as they are not fully independent from the statistical uncertainties.

We quantified the full systematic error budget as 0.68 * ($\sigma_{max} - \sigma_{min}$)/2, where σ_{max} and σ_{min} are the maximum and minimum σ obtained from all tests above (271 km/s, 403 km/s). The total uncertainties used for the analysis were then derived by adding statistical and systematic uncertainties in quadrature. The uncertainties for the velocities (redshifts) were estimated in the same way.

We used the systematic uncertainties derived for the integrated spectrum also for the individual spatial extractions, as we expect the template mismatch uncertainties to be of similar extent. In addition, to make sure that the result does not depend on a single line (e.g. due to residuals, etc.), we repeated the test excluding individual 1600km/s wide wavelength intervals in the fit of the individual spatial extractions. The uncertainties from this test were added additionally in squares.

The tilted absorption lines are not artifacts of the reduction

Due to the relatively small nod throws, the object itself can potentially contaminate the region used for background subtraction, especially in the outer parts. Therefore, we simulated the impact of the nodding strategy on the spatial profile and on the rotation curve. From this we conclude that we can safely use the rotation curve out to about 1".

As XSHOOTER is an echelle spectrograph, the geometrical mapping between the non-rectified and the rectified frame could potentially cause systematic effects, but we do not find any evidence of this. The residuals between predicted and actual positions of calibration lamp images do not deviate by more than one pixel and skylines are straight in the rectified output frames.

Another possible complication is the non-constant dark level of the NIR detector, especially variations between different rows of the detector, which transforms into half-circle like noise structures in the rectified frames. At the low S/N levels of the absorption lines, this may potentially conspire to make straight lines appear tilted. We simulated the appearance of straight lines on the detector in the rectified frames and did not find a clear correlation between the position of the half-circles and the observed absorption lines, arguing against this effect causing the tilt.

Finally the (tanh) rectification kernel could potentially cause problems; however, testing for this effect on several observed objects, we found significant effects only for point sources observed under very good seeing conditions.

Dynamical modeling

We model the rotation curve with a thin disk model with seven parameters46: the offset angle between the slit and the major axis of the disk (Θ_{off}), the disk inclination (i), the maximum velocity of the disk (V_{max}), the radius at which the disk reaches V_{max} (R_{max}), the position of the center of the slit relative to the disk center (X_c,Y_c), where a positive offset in both parameters indicates a slit center located to the northwest of the disk center, and an intrinsic velocity dispersion (σ_{int}), assumed to be constant across the disk.

We follow a standard Markov Chain Monte Carlo (MCMC) fitting approach with 100,000 iterations to find the combined best fit to the velocity and dispersion profiles. The fit employs a Metropolis-Hastings algorithm in which the proposed new value of each parameter is drawn from a Gaussian distribution centered at the current value and with a width drawn randomly from a specified range for each parameter. The allowed range was set empirically for each parameter to sample the posterior well while converging efficiently to a solution. The acceptance ratio α - defined as the ratio between the computed likelihoods for the proposed and previous models - was used to accept or reject the proposed model at each step. If α was greater than 1, indicating the proposed model was a better fit than the previous model, the proposed model was accepted; otherwise, the proposed new model was accepted only if α was greater than a random number drawn from a uniform distribution between 0 and 1. All parameters were varied simultaneously during the fitting and the first 10% of the iterations were treated as a burn-in period, and excluded from the final results.

During the fitting routine, each source plane model was convolved with a kernel that approximates the effects of seeing and lensing, weighted by the observed light profile of the galaxy and binned in the same way as the data. The dispersion measured for each model therefore includes the effects of velocity smearing as well as the intrinsic velocity dispersion, added in quadrature.

The single observed slit position angle limits our ability to break degeneracies among the parameters. However, our Galfit modeling provides firm constraints on the position and orientation of the galaxy with respect to the slit on the source plane, so we implement these as priors in the fit (Θ_{off} =22°±10°, $|x_c| < 0.4$ kpc). To speed up the fitting process, we also restrict the inclination to be within the range [45°,60°]. The posterior distributions for each parameter are shown in Extended Data Figure 8 as open histograms, along with the implied V_{max} / σ_{int} and dynamical mass $\left(M_{dyn} \sim V_{max}^2 r_e / G\right)$, where r_e is the measured effective radius. The filled histograms show the subset of fits with inclinations within 3σ of the inclination f implied by the measured axis ratio, assuming the disk is circular when viewed face-on. We adopt these distributions as our best fits, and list the median values and 68% confidence intervals for each parameter of the sampled models in Extended Data Table 2.

To test the effect of the assumed lensing and seeing kernel on the results, we repeated the analysis using four different kernels. Two represent the extreme ends of the magnification found among the 1979 realizations, and two represent the best and worst seeing plausible for our data. The results, summarized in Extended Data Table 2, are consistent with our benchmark model and show that lens model and seeing uncertainties are sub-dominant for our analysis when compared with observational uncertainties.

Spatially resolved stellar population characterization

The exquisite multi-band HST coverage, combined with the increased depth and resolution provided by the lensing, offers an opportunity to study trends in the spatially resolved stellar populations. To ensure sufficient S/N for robust stellar population characterization, we only

Europe PMC Funders Author Manuscripts

include the F850LP, F105W, F110W, F125W, F140W and F160W band images in the fits. The bluer bands are too shallow and noisy over most of the galaxy's extent to provide useful information. Next, we PSF-matched the images, and adaptively smoothed them, using ADAPTSMOOTH47,48. Smoothing masks were constructed for the reddest images (F125W, F140W and F160W), by requiring a minimum S/N=10 and a maximum smoothing radius of 3 pixels. These three masks were then combined and used to smooth all 6 images in the same way.

We then performed stellar population characterization for each pixel in the matched, smoothed images, and constructed 2D maps of stellar mass, age, extinction (Ai) and sSFR based on the median of their likelihood distributions (using the same technique as used in the benchmark fit of the spectrum). These maps were then transformed to the source plane using our well-constrained best-fit lensing model (Figure 3). Error maps were constructed from the 68% confidence intervals of the fits to the individual pixels.

In an absolute sense these parameters are subject to rather large uncertainties (see insets in Figure 3) due to age/dust/metallicity model degeneracies, however as individual spatial bins are independent (on scales larger than 3 pixels), the relative spatial structure is more robust, and the integrated properties are consistent with those derived from the full spectral fit.

In Extended Data Figure 3 we show radial profiles of the azimuthally averaged stellar population parameters (solid line). These show evidence for radial gradients with older stellar populations, higher extinction and lower sSFR in the center than in the outer parts. The shaded areas represent the pixel-to-pixel scatter in the median values in the elliptical apertures, not taking into account the uncertainties on the individual estimates.

The amplitudes of these regions provide a rough representation of the random errors on the parameters, i.e., due to measurement errors alone. (Note: this scatter slightly underestimates the real random error due to pixel-to-pixel correlation, e.g. because of the smoothing).

Also shown are the median-likelihood parameters values for the two spectral extractions, which are consistent with the photometric fits.

Despite the large systematic uncertainties, trends in physical parameters are evident and should be considered significant and robust under the hypothesis that there is no radial trend in the possible systematic bias affecting our estimates. Given the homogeneity of the observables throughout the radial extent of the galaxy and also the relatively small range in physical parameters, we have no reason to expect any radially varying systematic bias.

The gradients are not driven by the age/dust degeneracy as that would result in opposite slopes for age and dust profiles. Also shown is the average sSFR gradient derived from adaptive optics observations of similar mass z=2 star forming galaxies23, which has been interpreted as evidence of inside out morphological quenching. The sSFR gradient in MACS2129-1 has a similar shape, but is depressed by a factor of >100.

The observed age gradient suggests that quenching in MACS2129-1 proceeded inside out, over a timescale of ~300 Myr.

Inspection of the maps shows an off-center clump, with a younger stellar population and less extinction than the rest of the galaxy. This may indicate an ongoing minor merger, but we cannot confirm this as it is not detected in the spectrum. Masking out the clump does not change the derived radial stellar population gradients significantly.

Surface Brightness fits

We used Galfit49 to fit the source plane F160W (restframe optical) 2D surface brightness profile with a Sersic model. As a PSF model we used a point source, reconstructed on the source plane in the same way as MACS2129-1 (see inset in Figure 2). In addition to the formal fitting errors, uncertainties in the lensing model used for source plane reconstruction must be taken into account.

We do this by re-running Galfit on 98 different reconstructed images and matching PSFs, selected to sample the full range of lensing model realizations.

The derived parameters are very stable (see Extended Data Figure 6), with mean and standard deviations of r_e =20.9 ± 0.6 pixel, a/b=0.59 ± 0.01, $r_{e,cir}$=1.73 ± 0.05 kpc, n=1.01 ± 0.01, pa=-45.17±0.96 deg., demonstrating that lensing model uncertainties do not significantly affect the shape and orientation of the galaxy on the source plane. The main potential systematic uncertainty on our lens modeling is associated with the implementation of substructure. As a conservative upper limit on this uncertainty, we repeated the Galfit analysis on two extreme sets of model realization. One where the nearby cluster galaxy has zero mass and one where it has twice the mass. In the first case we obtain r_e =24.9 ± 0.6 pixel, a/b=0.49 ± 0.01, $r_{e,cir}$=1.89 ± 0.03 kpc, n=0.89 ± 0.01, pa=-35.49±0.38 deg, in the second r_e =18.2 ± 0.5 pixel, a/b=0.62 ± 0.01, $r_{e,cir}$= 1.55± 0.04 kpc, n=1.07 ± 0.01, pa=-58.0±1.8 deg.

From these tests we derive conservative estimates of the total errors (statistical and maximum systematic added in quadrature) for the Galfit parameters: $r_e = 20.9^{+4.0}_{-2.8}$ pixel, $a/b = 0.59^{+0.03}_{-0.09}$, $r_{e,cir} = 1.73^{+0.34}_{-0.27}$ kpc, $n = 1.01^{+0.12}_{-0.06}$, $pa = -45.0^{+9.8}_{-12.8}$ deg. We also repeated the dynamical modeling with these models, but found no significant changes in the results. This analysis is sensitive only to the brightest, central part of the galaxy which is not very strongly affected by the substructure, and its error budget is dominated by the limited S/N of the spectrum, and PSF smearing.

Finally we note that masking out the north-east clump does not change the 2D fit or the 1D profile significantly. It is thus not the main source of the “excess light” seen at large radii.

To test what structural parameters we would have derived for MACS2129-1 in the absence of lensing we repeated our Galfit analysis on a “de-lensed” version of the source plane F160W image. This image was created by re-binning the F160W source plane image to the pixel scale of WFC3, convolving it with the WFC3 PSF, scaling its brightness by the inverse of the magnification factor and inserting it into an empty region of the original F160W image. The best fitting parameters $r_{e,cir}$=1.92 ± 0.02 kpc, n=1.02 ± 0.03 are similar, demonstrating that MACS2129-1 would have been identified as a compact exponential disk, even in the absence of lensing.

Emission lines: AGN outflow?

We decompose the stellar continuum and nebular emission lines in the VIS-NIR spectrum using pPXF+Gandalf50. Detected lines in the central and outer extractions are listed in Extended Data Table 1. The emission lines are centrally concentrated. To estimate the hardness of the ionizing field, we calculate the line ratios log([NII]/H_α) = −0.06 ± 0.10, log([OIII]/H_β) > 0.45 ± 0.08. The latter is a lower bound, since H_β is undetected, and estimated assuming case B recombination (H_α/H_β=2.9) and no extinction. These ratios are inconsistent with OB stars being the main ionizing source, but consistent with the expectations from AGN or a LINERs18. The emission lines have dispersions similar to those measured from the absorption lines (σ_{em} = 382 km/s), but are redshifted by 238 km/s. Velocity offsets of this order are expected from bipolar AGN outflows. Usually these are blue shifted, but in some local Seyfert galaxies redshifted lines are observed, when the angle of the bicone outflow is small with respect to the main plane of the host galaxy51.

Alternatively, the redshift could be caused by spatially unresolved patchy star formation or dust in the inner part of the disk, but since the emission is centrally concentrated and the line ratios suggest AGN origin, this is a less likely scenario.

An exotic interpretation of the weak redshifted emission lines is that MACS2129-1 is a high redshift analog of the so-called "offset AGN", observed in a significant fraction of local early type or post-merger galaxies in over dense environments52.

The offsets in these are interpreted as being due to dual black holes where only one of them is accreting; a sign post of a major merger in the recent past52. Simulations show that if the merger was gas rich (gas fraction > 0.5) it would have commenced 1-2 Gyr earlier53, and that the gas in the remnant under such conditions can quickly rearrange itself in a rapidly spinning central disk54. This is a plausible alternative formation scenario for the massive stellar disk observed in MACS2129-1, consistent with its mean stellar age (~750Myr).

How common is rotation in quiescent galaxies?

The exponential profile and late type kinematics of MACS2129-1 appear in tension with the commonly accepted picture derived from lower resolution data, that high redshift quiescent galaxies are predominantly dispersion dominated6 proto bulges with de Vaucouleurs like profiles55. A picture that provides a straightforward link to their low redshift descendants5. However there is a growing body of indirect evidence that quiescent galaxies may grow more "disky" and rotation dominated with redshift. A number of studies have found a fraction of quiescent galaxies to have exponential disk like surface brightness profiles, both at high11,13,56,57 and intermediate redshifts58. Indeed, the best candidate low redshift direct descendant of a z=2 cQG was found to be a rapidly rotating exponential disk59. Also, it has been argued that the average observed axis ratios of z~2 cQGs are consistent with the majority of them being disks60.

Recently it was argued that dynamical mass of z~2 quiescent galaxies with exponential disk like profiles, calculated from unresolved spectroscopy was higher than expected from their stellar mass, which was interpreted as evidence for unresolved rotation13. The resolved kinematics for MACS2129-1 allows us to test this interpretation. If we calculate the dynamical mass in the same way as this study $log\,M_{dyn}(\sigma_e) = \beta(n)\,\sigma_e^2\,r_{e,Maj}/G$, where $\beta(n) = 8.87 - 0.831n - 0.024n^2$, n is the Sersic index, σ_e is the spatially integrated velocity dispersion, and $r_{e,Maj}$ is the major axis effective radius, we find $logM_{dyn}(\sigma_e) = 11.65 \pm 0.14$, a factor of 2 higher than the total dynamical mass derived from resolved kinematics $logM_{dyn,tot}(V_{rot}) = 11.30 \pm 0.14$ (assuming that $logM_{dyn,tot}(V_{rot}) = 2 * logM_{dyn,r<re}(V_{rot})$). In the framework of the aforementioned study, the implied $\log(M_*/M_{dyn}) = -0.39 \pm 0.37$ suggest a contribution from unresolved rotation up to V/σ~3, however given the error bars, the result is not statistically significant. We note that assuming $\beta = 5$, and $r_{e,c}$ instead of $r_{e,Maj}$ as commonly done in the literature, brings the unresolved $log\,M_{dyn}(\sigma_e) = 5\,\sigma_e^2\,r_{e,c}/G = 11.33 \pm 0.09$ in perfect agreement with that derived from the resolved kinematics.

Gravitational lensing offers the currently best way to directly quantify the ubiquity of rotation in high redshift quenched galaxies until we have the ELTs. Ground based AO observations with 8-10 m telescopes can in principle resolve un-lensed examples, but will struggle with sensitivity when the signal is spread out. JWST will have the sensitivity required, but not quite the spatial resolution.

So far three gravitationally lensed quiescent galaxies have been studied spectroscopically, MACS2129-1 (z=2.1), RG1M0150 (z=2.6) and COSMOS 0050+4901 (z=2.8). The first two show clear evidence of rotation, the third did not have sufficient S/N to tell61

Gravitational lensing of quiescent galaxies is a rare phenomenon, but with systematic investigation of the large number of massive clusters available from existing and future surveys, it will be possible to build statistical samples of quiescent galaxies with resolved spectroscopy, one galaxy at a time.

SFR limit from Spitzer/MIPS

We derive an upper limit on the SFR in MACS2129-1 from its non-detection by Spitzer/MIPS at 24μm (PI: Yun). From the RMS of the 24μm map we derive a 3σ upper limit of f_{24}=45μJy. We convert this to an upper limit of LIR < $(2.3 \pm 2.0) \cdot 10^{11} L_\Theta$, by assuming various templates (e.g. MS and SB templates from Magdis 2012, M82 and Arp220). We then correct for magnification and derive an upper limit on the star formation rate SFR < 5 M_Θ/yr, using the Kennicutt17 relation (modified to a Chabrier IMF).

Code Availability

The code used to perform the stellar population characterization from the XSHOOTER spectrum and the multi-band photometry is not publicly available, since full user documentation and interface are not yet developed. The base SSP models adopted are publicly available at http://www.iap.fr/~charlot/bc2003. The adopted SFH library and the

Bayesian fitting approach are fully described in Zibetti al et 201743, available at https://arxiv.org/abs/1701.06570.

The code ADAPTSMOOTH47,48, used to PSF-match and adaptively smooth the images, is available at http://www.arcetri.astro.it/~zibetti/Software/ADAPTSMOOTH.html. The codes, pPXF16 in combination with GANDALF50, used to decompose the stellar continuum and the nebular emission lines in the X-Shooter spectrum is publicly available at http://www-astro.physics.ox.ac.uk/~mxc/software/. We also made use of pPXF with a simple wrapping script (available upon request), for measuring the galaxies kinematics.

Cluster mass modeling and source reconstructions are made using the latest version of the software Lenstool, which is publicly available at the following web page: https://projets.lam.fr/projects/lenstool/wiki. The parameter file for Lenstool is available upon request.

The code used to perform the MCMC disk fitting analysis is not publicly available, since user documentation is not yet developed, but is described in detail in Prescott et al.46.

Data Availability

This paper is based on observations made with ESO telescopes at the La Silla Paranal Observatory under Programme 087.B-0812(B), which are publically available at http://archive.eso.org. It also employs HST data from the CLASH survey (Prog. ID 12460), which is publically available at http://archive.stsci.edu/hst/. The reduced XSHOOTER 2D spectrum used the kinematic analysis and the binned 1D spectrum used for the stellar population synthesis analysis is available at https://sid.erda.dk/sharelink/g9s5FnqZjT.

The best fitting stellar population model to the full XSHOOTER spectrum is available on request.

Extended Data

Europe PMC Funders Author Manuscripts

Europe PMC Funders Author Manuscripts

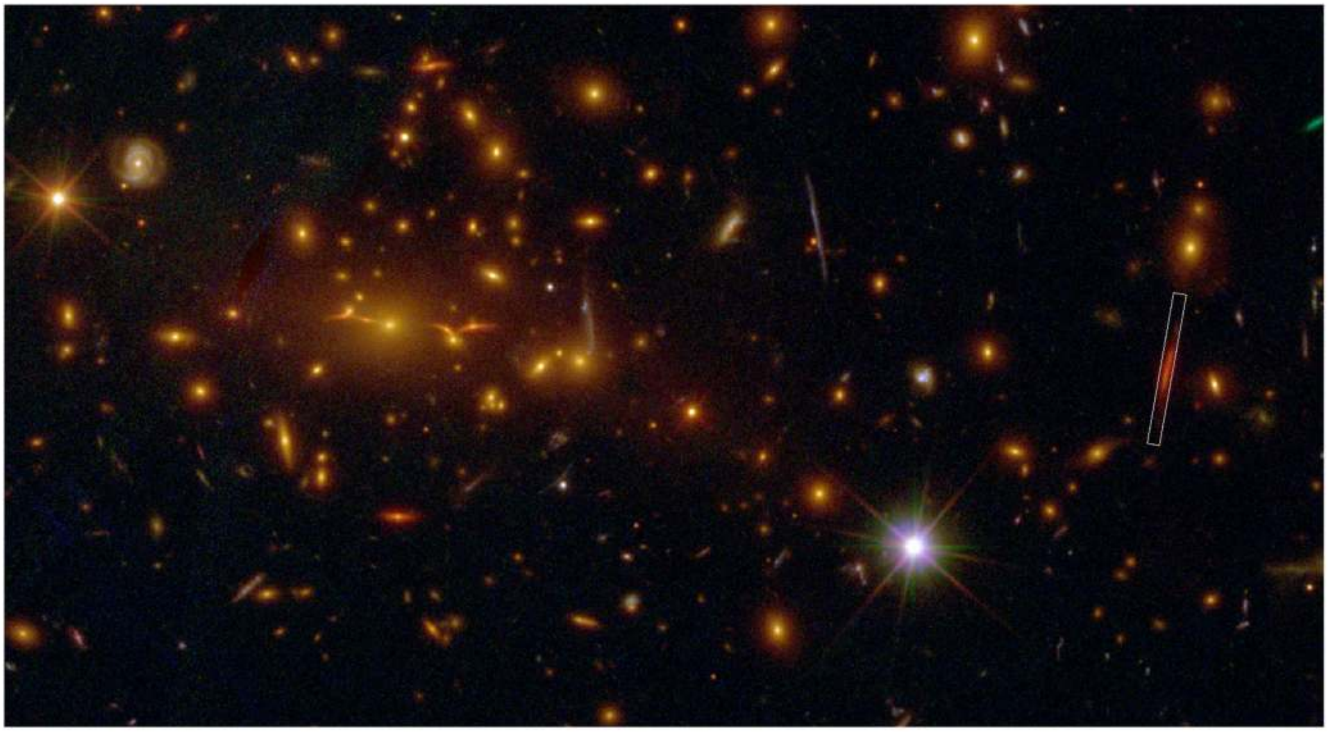

Extended Data Figure 1.

Hubble color image of the lensing cluster MACS2129-0741. Indicated is the position of the X-shooter slit on the target, which has been magnified and stretched by an average factor of ~4.6 by the foreground cluster. The image is a color composite (B = F435W + F475W; G = F555W + F606W + F775W + F814W + F850LP; R = F105W + F110W + F125W + F140W + F160W) constructed from CLASH data62.

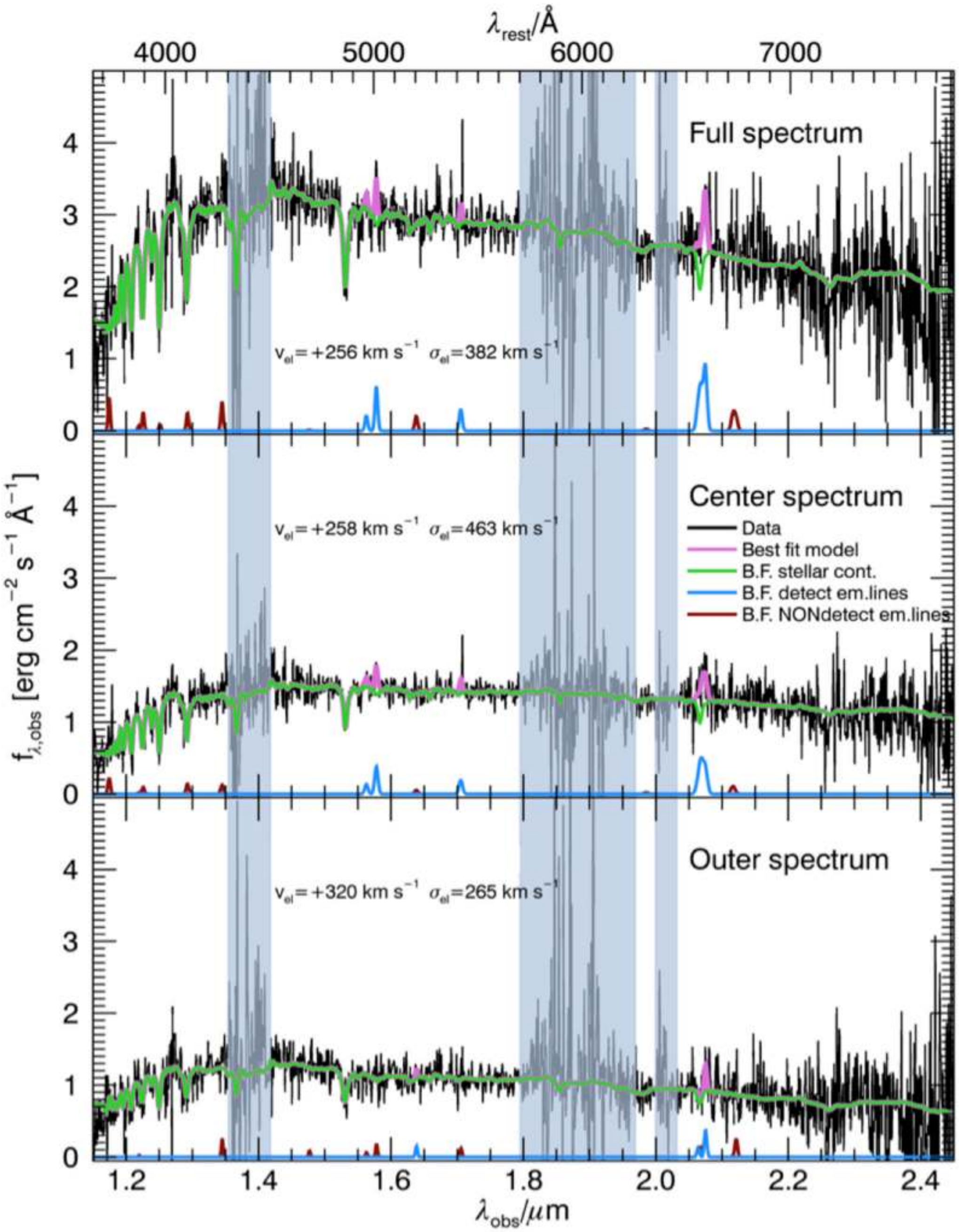

Extended Data Figure 2.

Emission line characterization in three spatial extractions of the XSHOOTER spectrum. The top/middle/bottom panels show the full (|r| < 1.36")/ central (|r| < 0.5")/outer (0.5" < |r| < 1.36") extractions, respectively. The colored lines represent spectral decomposition into nebular emission lines and stellar continuum, obtained with pPXF/GANDALF50: the orchid line displays the best fitting composite model; the green line is the best fitting stellar continuum; the blue and dark red lines represent the best fitting emission lines with and without a significant detection, respectively. Shaded regions indicate spectral regions of low atmospheric transmission/high background that have been excluded from the fit.

Europe PMC Funders Author Manuscripts

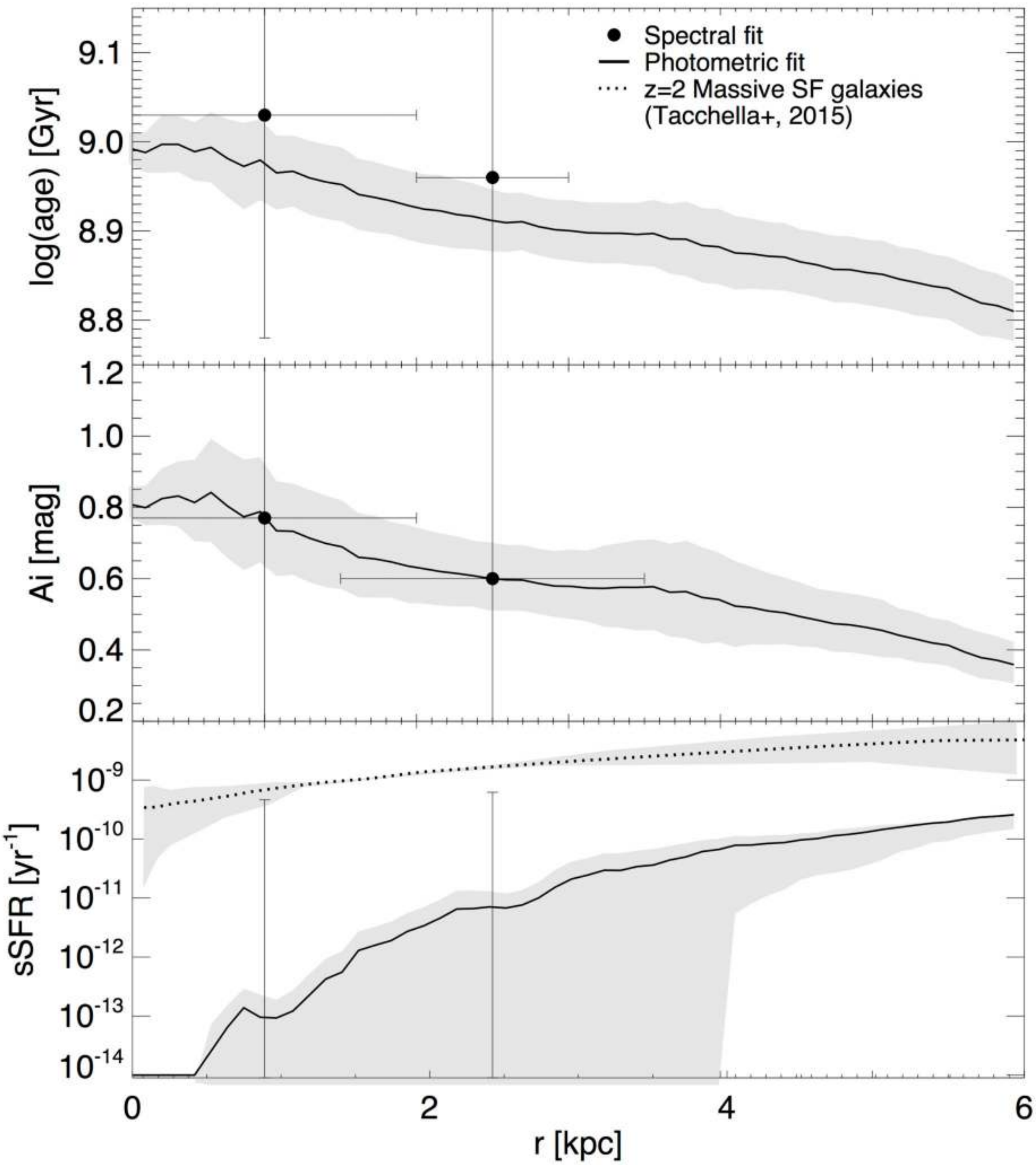

Extended Data Figure 3.

Radial stellar population gradients. The full lines show azimuthally averaged radial profiles of median likelihood stellar population synthesis parameters, derived from the maps in Figure 3 in elliptical apertures following the best fitting 2D surface brightness fit. The error bars represent the standard deviation of the best fitting values in the apertures, not the absolute errors on the individual fits. The filled circles show results from the spectral fits, with absolute error bars. The dotted line shows the average sSFR profile from a sample of star forming galaxies23 of similar mass and redshift as MACS2129-1

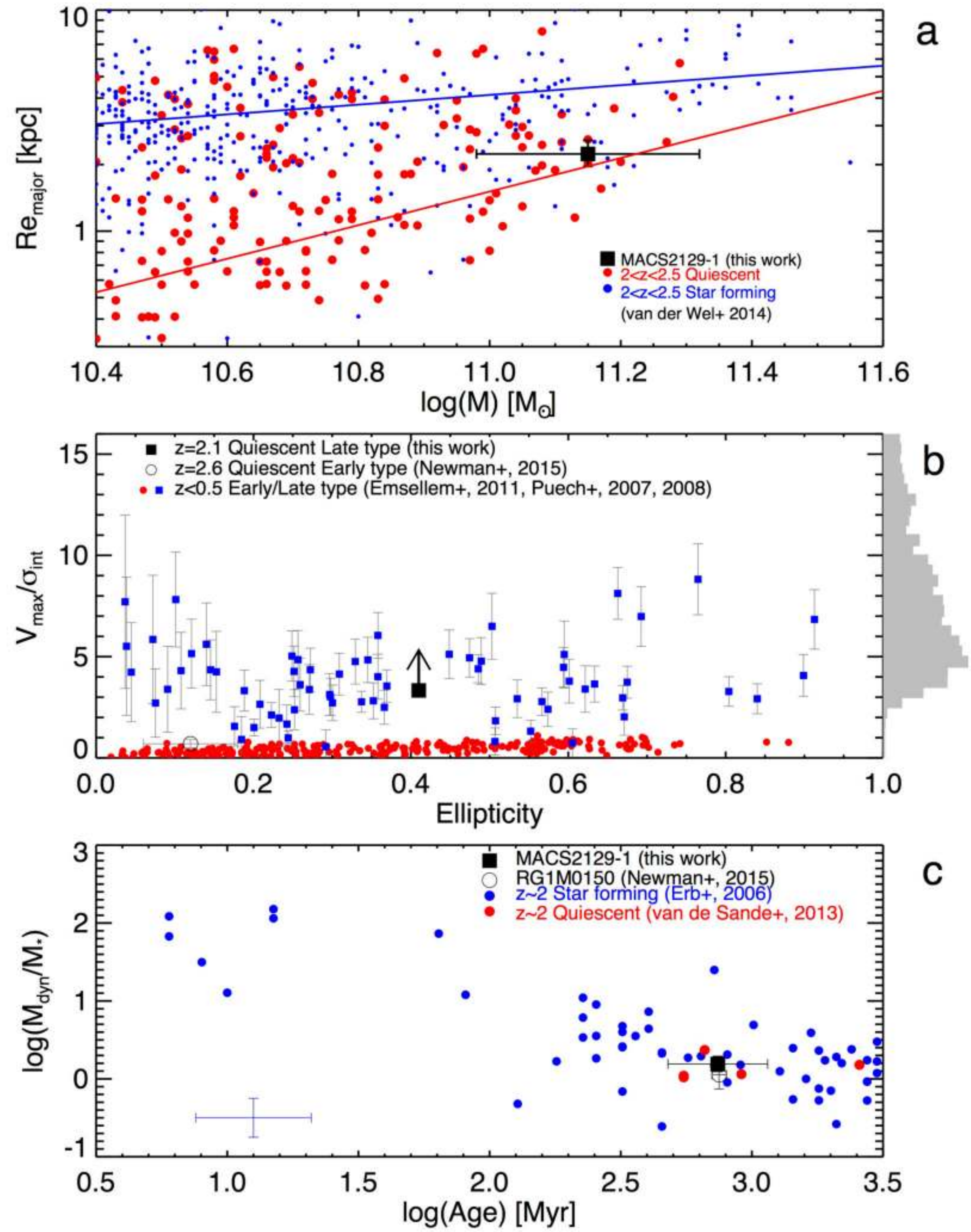

Extended Data Figure 4.

Properties of MACS2129-1 compared to different galaxy populations. a) Stellar masses and sizes of 2<z<2.5 galaxies in the CANDELS survey2. MACS2129-1 (black square) falls on the relation for quiescent galaxies, b) $\mathbf{V_{max}/\sigma_{int}}$ versus ellipticity for the two lensed z>2 cQGs MACS2129-1 and RG1M0150 compared to similar mass local galaxies. The grey histogram shows the $\mathbf{V/\sigma}$ posterior distribution from our modeling. MACS2129-1 is thus similar to local late types62,63 (blue), while RG1M0150 is similar to local early types (red). c) The dynamical to stellar mass ratio (within re) of MACS2129 is similar to previously observed z>2 cQGs, including the strongly lensed RG1M0150, and to z~2 star-forming galaxies of similar age49.

Europe PMC Funders Author Manuscripts

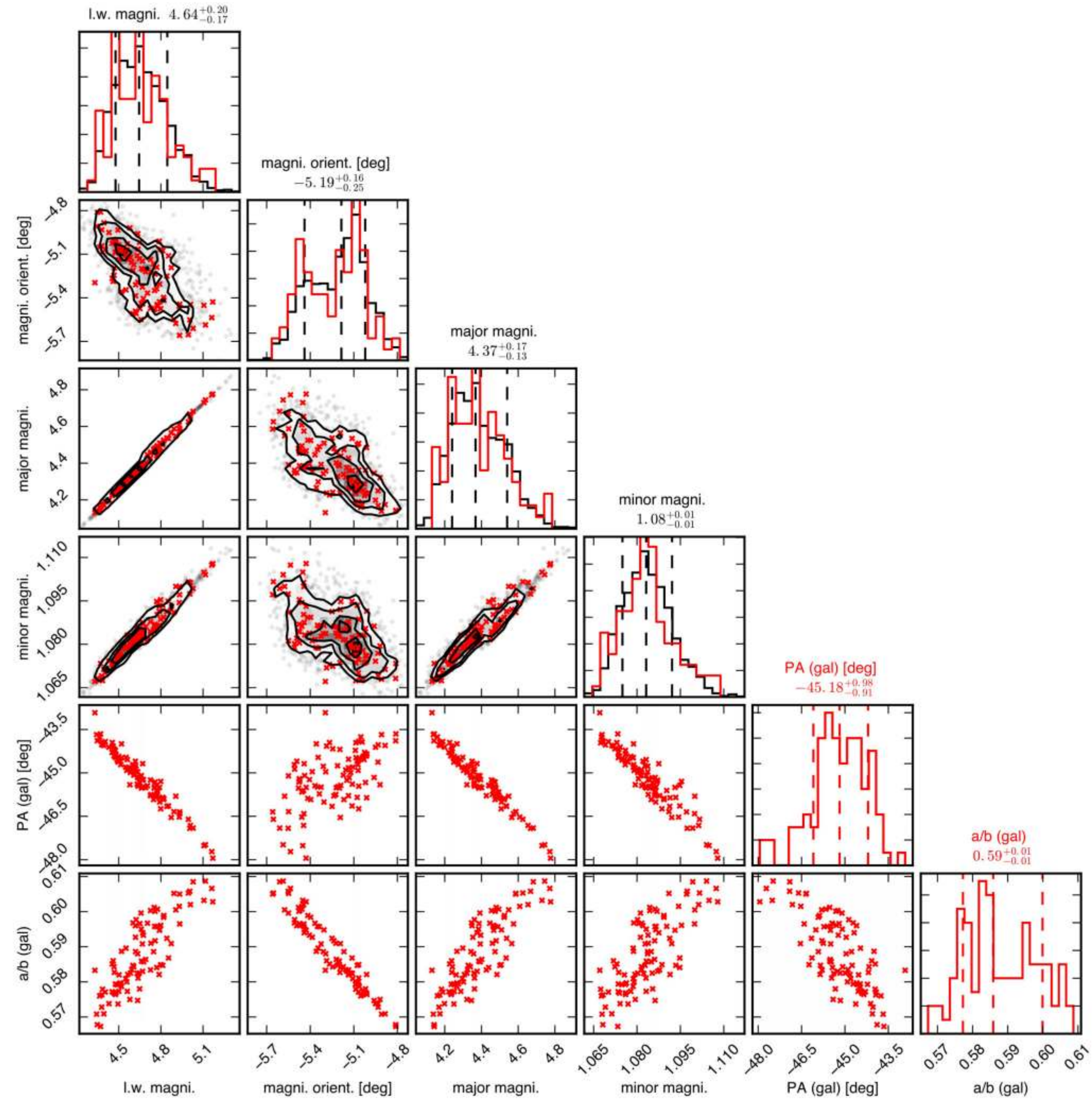

Extended Data Figure 5.

Correlations between lensing model parameters and derived structural parameters for MACS2129-1. Shown are the average light weighted (l.w.) magnification, the direction of maximum magnification at the position of MACS2129-1, the magnification along this axis (major. magni.) and perpendicular to it (minor magni.). These were obtained from 1979 lensing model realizations (black) sampling the full probability distribution. Also shown are correlations with the galaxy axis ratios (a/b) and position angles (PA) of MACS2129-1 derived from Galfit analysis of reconstructed source plane images for a subsample of 98 representative realizations (red).

Europe PMC Funders Author Manuscripts

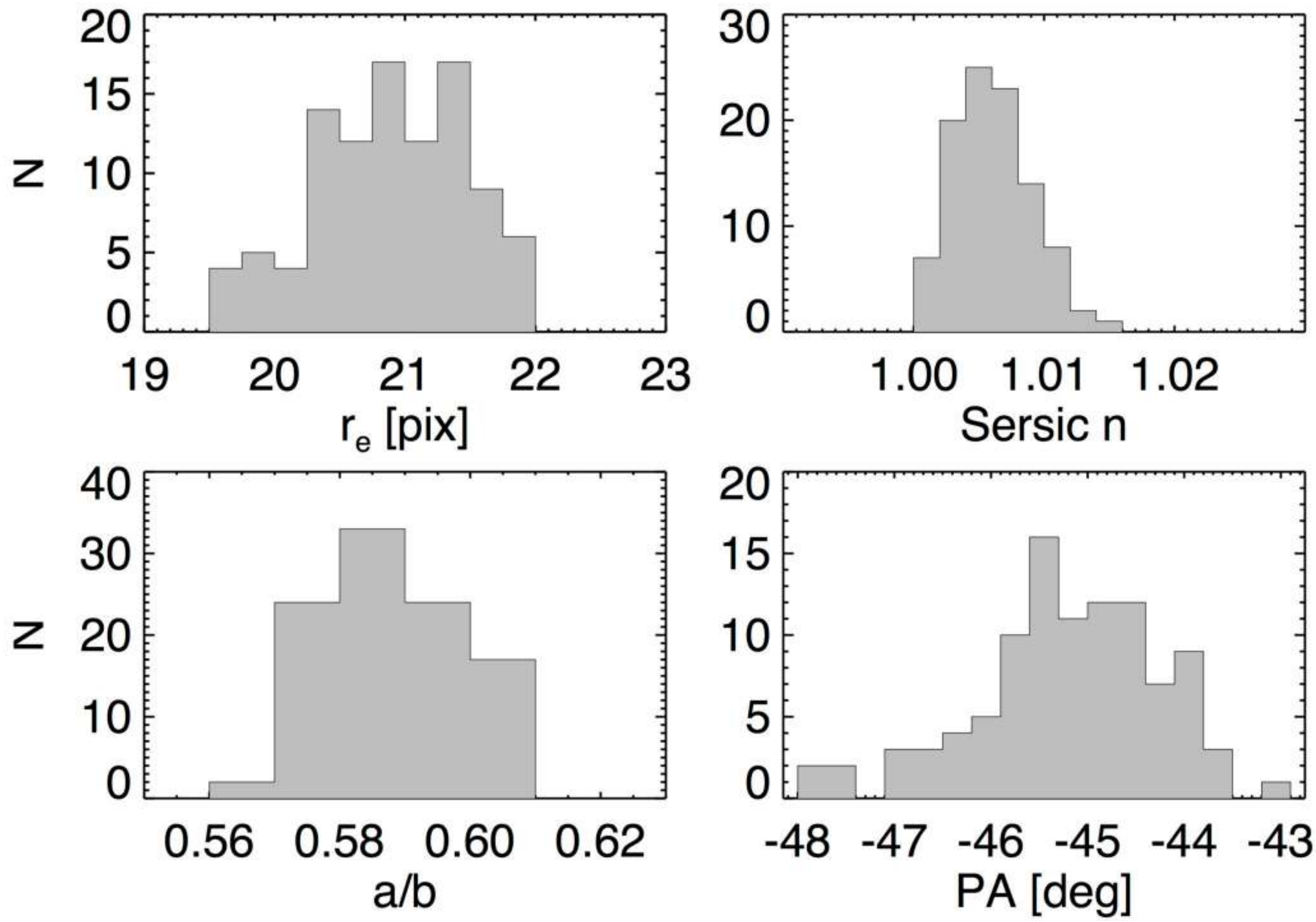

Extended data Figure 6.
Structural parameters. Distribution of Sersic model parameters derived from 2D surface brightness fits with Galfit, on the source plane images generated from 98 representative realizations of the lensing model. We adopt the median values of these distributions and their standard deviations as our best fitting parameters.

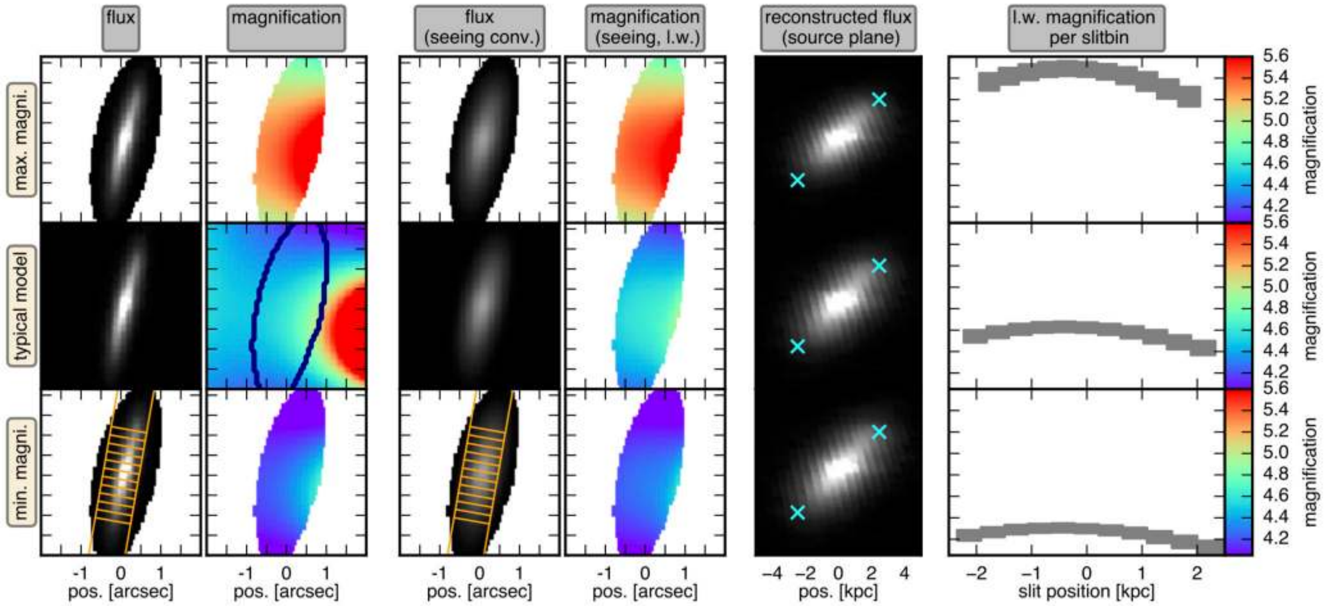

Extended data Figure 7.

Variations of the magnification over MACS2129-1. Results are shown for a typical realization (middle), and for the realizations with the maximum (top) and minimum (bottom) magnifications. The columns (from left to right) show 1: Observed F160W image, 2: Magnification map, 3: Seeing convolved (FWHM=0.5”) F160W image, 4: Seeing convolved light (F160W) weighted magnification map, 5: source plane image (crosses at same position) 6: Average, light weighted magnification contributing to each spatial bin in the XSHOOTER slit (shown in the bottom row). The minor variations are caused by the galaxy 3.5 arcsec west of MACS2129-1 (see middle row).

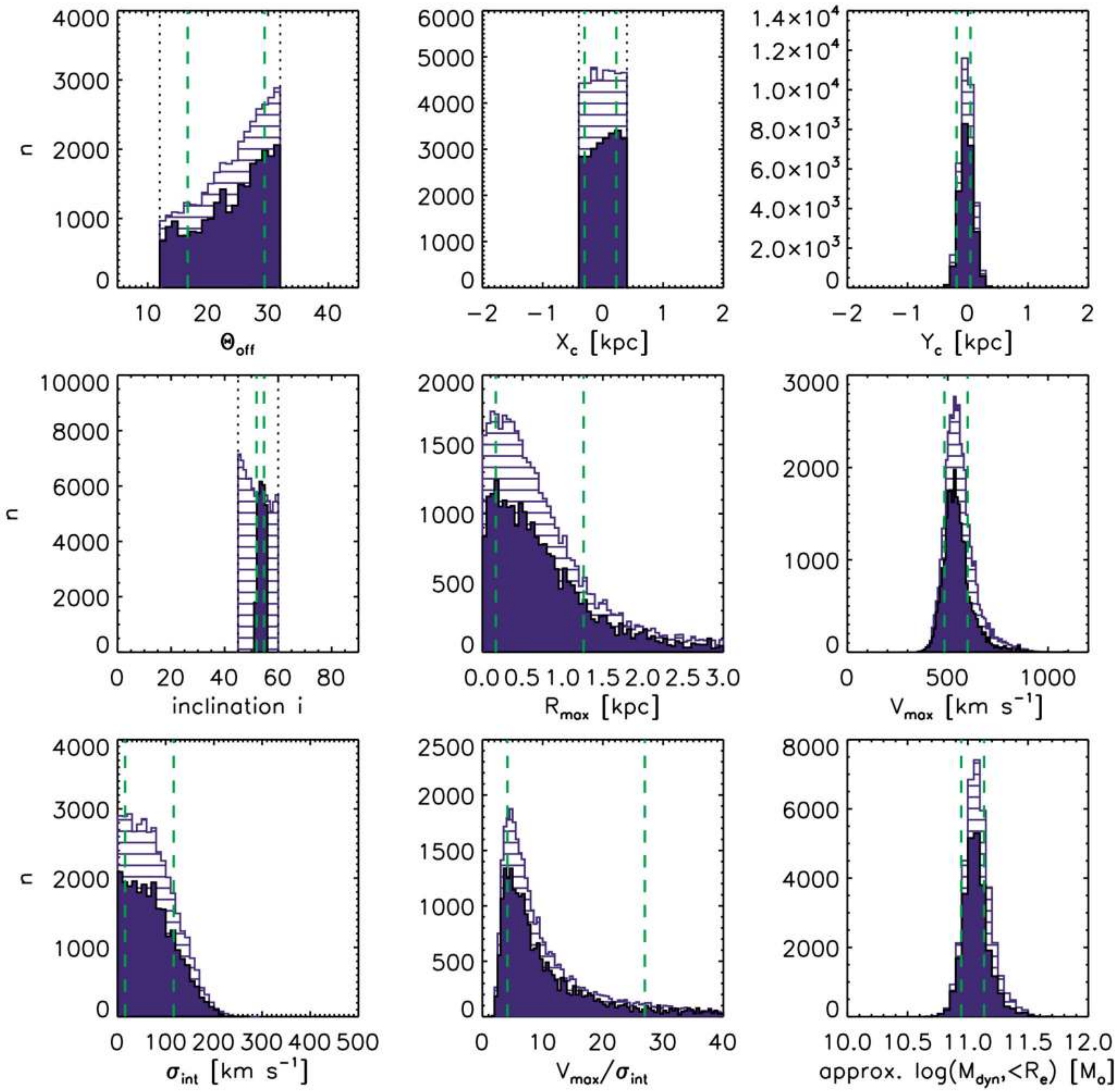

Extended data Figure 8.

Posterior distributions for the parameters in our dynamical modeling of the rotation and dispersion curves. The open histograms show the distributions with priors $\mathbf{\Theta_{off} = 22 \pm 10}$°, $|$ $\boldsymbol{X_c}|$ **<0.4″**. Filled histograms with the additional prior $\boldsymbol{i}$ **= 53.8** ± **2.13**°, all derived from Galfit modeling.

Europe PMC Funders Author Manuscripts

Extended Data Table 1

Stellar population parameters and emission line fluxes. a: Median likelihood and 16-84% confidence intervals for the parameters of our stellar population characterization of MACS2129-1. The age and mettalicity are light weighted. The SFR is the mean over the last 10^7 years. SFR and M* are corrected for magnification. Library A is our default library, while Library B includes only models without additional random burst of star formation. Fit1 is performed on the whole XSHOOTER spectrum pixel-by-pixel, while Fit2 is performed on absorption line indices and optical-NIR-MIR photometry. b: Median likelihood and 16-84% confidence intervals for the parameters of our stellar population characterization of MACS2129-1 using LibraryA/Fit1, for a central and an outer extraction. c: Detected emission line fluxes, widths and systematic velocity offsets (relative to the absorption lines), in three spatial extraction of the XSHOOTER spectrum (see Extended Data Figure 2).

a

	Library A, Fitl	**Library B, Fit1**	**Library A, Fit2**	**Library B, Fit2**
Log(Age/yr)	$8.97^{+0.26}_{-0.25}$	$9.02^{+0.25}_{-0.25}$	$8.87^{+0.25}_{-0.19}$	$8.86^{+0.23}_{-0.17}$
Log($Z/Z_\odot$)	$-0.56^{+0.55}_{-0.55}$	$-0.58^{+0.54}_{-0.53}$	$-0.53^{+0.53}_{-0.53}$	$-0.51^{+0.51}_{-0.56}$
A_i [mag]	$0.60^{+0.90}_{-0.60}$	$0.33^{+0.88}_{-0.33}$	$0.73^{+0.73}_{-0.71}$	$0.70^{+0.53}_{-0.70}$
Log($M^*/M_\odot$)	$11.15^{+0.23}_{-0.20}$	$11.10^{+0.26}_{-0.20}$	$11.05^{+0.19}_{-0.16}$	$11.03^{+0.19}_{-0.16}$
SFR [$M_\odot/10^7$yr]	$0.0^{+139.6}_{-0.0}$	$0.0^{+0.2}_{-0.0}$	$0.9^{+86.1}_{-0.9}$	$0.5^{+14.1}_{-0.5}$

b

	Center (|r|<0.5”)	**Outer (0.5” < |r| < 1.4”)**
Log(Age/yr)	$9.03^{+0.24}_{-0.28}$	$8.96^{+0.27}_{-0.26}$
Log($Z/Z_\odot$)	$-0.49^{+0.56}_{-0.55}$	$-0.56^{+0.57}_{-0.56}$
A_i [mag]	$0.77^{+0.94}_{-0.75}$	$0.60^{+0.98}_{-0.60}$
sSFR [yr^{-1}]	$0.0^{+4.6e-10}_{-0.0}$	$0.0^{+6.2e-10}_{-0.0}$

c

	[OIII]$_{5007}$ [erg/s/cm^2]	**HeII$_{5411}$ [erg/s/cm^2]**	**Hα_{6563} [erg/s/cm^2]**	**[NI]$_{5198}$ [erg/s/cm^2]**	**[NII]$_{6583}$ [erg/s/cm^2]**	**σ [km/s]**	**Vsys [km/s]**
Total	2.8±0.3	1.4±0.3	3.3±0.8	1.0±0.3	5.3±0.7	382	236

c

	[OIII]$_{5007}$ [erg/s/cm^2]	**HeII$_{5411}$ [erg/s/cm^2]**	**Hα_{6563} [erg/s/cm^2]**	**[NI]$_{5198}$ [erg/s/cm^2]**	**[NII]$_{6583}$ [erg/s/cm^2]**	**σ [km/s]**	**Vsys [km/s]**
Central	2.1±0.2	1.1±0.2	2.9±0.5	-	2.5±0.5	463	258
Outer	-	-	-	0.5±0.2	1.5±0.4	265	320

Europe PMC Funders Author Manuscripts

Extended Data Table 2

Dynamical modeling results. a: Dynamical modeling results from our benchmark model. b: Dynamical modeling results, using four different realizations of the seeing+lensing kernels spanning the extreme highest and lowest magnifications found in our 1979 realizations, and the worst and best seeing allowed by our data.

a

Parameter	Median	67% Confidence
Θ_{off} [deg]	26.4	[16.6, 29.4]
Inclination [deg]	53.8	[51.9, 54.7]
R_{max} [kpc]	0.5	[0.2, 1.3]
V_{max} [km/s]	532	[483, 599]
X_c [kpc]	0.0	[-0.3, 0.2]
Y_c [kpc]	0.0	[-0.2, 0.0]
σ_{intr} [km/s]	59	[16,116]
V_{max} / σ_{intr}	22	[4,27]
$Log(M_{dyn}/M_{\odot})$	11.0	[10.9, 11.1]

b

Model realizations	V_{max}[km/s]	R_{max}[kpc]	σ_{intr} [km/s]	V_{max} / σ_{intr}
Benchmark	523^{+67}_{-49}	$0.5^{+0.8}_{-0.3}$	59^{+57}_{-44}	22^{+5}_{-18}
Max magnification	524^{+52}_{-54}	$0.4^{+0.7}_{-0.3}$	62^{+57}_{-44}	24^{+2}_{-20}
Min magnification	539^{+67}_{-55}	$0.5^{+0.8}_{-0.3}$	55^{+59}_{-39}	23^{+3}_{-18}
Max seeing	543^{+80}_{-50}	$0.6^{+0.9}_{-0.4}$	49^{+55}_{-36}	28^{+3}_{-23}
Min seeing	517^{+51}_{-52}	$0.4^{+0.6}_{-0.3}$	77^{+51}_{-54}	14^{+5}_{-10}

Acknowledgements

ST,GM,NL,CGG and MS acknowledges support from the ERC Consolidator Grant funding scheme (project ConTExt, grant number: 648179). CG acknowledges support by VILLUM FONDEN Young Investigator Programme (grant no. 10123). GM acknowledge support from the Carlsberg Foundation and by VILLUM FONDEN Young Investigator Programme (grant no. 13160). S.Z. and A.G. acknowledge support by the EU Marie Curie Career Integration Grant "SteMaGE" Nr. PCIG12-GA-2012-326466 (Call Identifier: FP7-PEOPLE-2012 CIG). We thank Min Yun and Ryan Cybalski for providing the deep Spitzer data, and Darach Watson and Francesco Valentino for insightful discussions.

References

1. Ilbert O, et al. Mass assembly in quiescent and star-forming galaxies since z ≃ 4 from UltraVISTA. Astron Astrophys. 2013; 556:A55.
2. van der Wel A, et al. 3D-HST+CANDELS: The Evolution of the Galaxy Size-Mass Distribution since z = 3. Astrophys J. 2014; 788:28.
3. van de Sande, et al. Stellar Kinematics of z ~ 2 Galaxies and the Inside-out Growth of Quiescent Galaxies. Astrophys J. 2013; 771:85.

Europe PMC Funders Author Manuscripts

4. Toft S, et al. Deep Absorption Line Studies of Quiescent Galaxies at z ~ 2: The Dynamical-mass-Size Relation and First Constraints on the Fundamental Plane. Astrophys J. 2012; 754:3.
5. Toft S, et al. Submillimeter Galaxies as Progenitors of Compact Quiescent Galaxies. Astrophys J. 2014; 782:68.
6. Hopkins P, et al. Compact high-redshift galaxies are the cores of the most massive present-day spheroids. Mon Not R Ast Soc. 2009; 398:898–910.
7. Newman AB, Belli S, Ellis RS. Discovery of a Strongly Lensed Massive Quiescent Galaxy at z = 2.636: Spatially Resolved Spectroscopy and Indications of Rotation. Astrophys J. 2015; 813:7.
8. Wuyts S, et al. On Sizes, Kinematics, M/L Gradients, and Light Profiles of Massive Compact Galaxies at z ~ 2. Astrophys J. 2010; 722:1666–1684.
9. Dekel A, et al. Galaxy bimodality due to cold flows and shock heating. Mon Not R Ast Soc. 2006; 368:2–20.
10. Toft S, et al. Hubble Space Telescope and Spitzer Imaging of Red and Blue Galaxies at z ~ 2.5: A Correlation between Size and Star Formation Activity from Compact Quiescent Galaxies to Extended Star-forming Galaxies. Astrophys J. 2007; 671:285–302.
11. Van Dokkum P, et al. Confirmation of the Remarkable Compactness of Massive Quiescent Galaxies at z ~ 2.3: Early-Type Galaxies Did not Form in a Simple Monolithic Collapse. Astrophys J. 2008; 677:5.
12. van der Wel A, et al. The Majority of Compact Massive Galaxies at z ~ 2 are Disk Dominated. Astrophys J. 2011; 730:38.
13. Belli S, et al. MOSFIRE Spectroscopy of Quiescent Galaxies at 1.5 < z < 2.5. I – Evolution of Structural and Dynamical Properties. Astrophys J. 2017; 834:18.
14. Naab T, et al. The ATLAS^{3D} project - XXV. Two-dimensional kinematic analysis of simulated galaxies and the cosmological origin of fast and slow rotators. Mon Not R Ast Soc. 2014; 444:3357–3387.
15. Ebeling H, Edge AC, Henry P. MACS: A Quest for the Most Massive Galaxy Clusters in the Universe. Astron J. 2001; 553:668–676.
16. Cappellari M. Improving the full spectrum fitting method: accurate convolution with Gauss-Hermite functions. Mon Not R Ast Soc. 2017; 466:798–811.
17. Kennicutt RC Jr. The Global Schmidt Law in Star-Forming Galaxies. Astrophys J. 1998; 498:541–552.
18. Kewley LJ. Theoretical Modeling of Starburst Galaxies. Astrophys J. 2001; 556:121–140.
19. Yesuf HM. From Starburst to Quiescense: Testing Active Galactic Nucleus in Rapidly Quenching Post-starburst Galaxies. Astrophys J. 2014; 792:84.
20. Whitaker K, et al. Constraining the Low-Mass Slope of the Star Formation Sequence at 0.5<z<2.5. Astrophys J. 2014; 795:104.
21. Emsellem E, et al. The SAURON project – IX. A Kinematic Classification for Early-type Galaxies. Mon Not R Ast Soc. 2007; 379:401–417.
22. Puech M, et al. 3D Spectroscopy with VLT/GIRAFFE. IV. Angular momentum and. Astron Astrophys. 2007; 466:83–92.
23. Tacchella S, et al. Evidence for Mature Bulges and an Inside-out Quenching Phase 3 billion years after the Big Bang. Science. 2015; 348:314. [PubMed: 25883353]
24. Behroozi P, Wehcsler, Conroy. The average star formation histories of galaxies in dark matter halos from z=0-8. Astrophys J. 2013; 770:57.
25. Croton D, et al. The many lives of active galactic nuclei: cooling flows, black holes and the luminosities and colours of galaxies. Mon Not R Ast Soc. 2006; 365:11–28.
26. Oteo I, et al. Witnessing the birth of the red sequence: ALMA high-resolution imaging of [CII] and dust in two interacting ultra-red starbursts at z = 4.425. Astrophys J. 2016; 827:34.
27. Riechers D, et al. ALMA Imaging of Gas and Dust in a Galaxy Protocluster at Redshift 5.3: [C II] Emission in “Typical” Galaxies and Dusty Starbursts ≈1 Billion Years after the Big Bang. Astrophys J. 2014; 796:84.
28. Barro G, et al. Keck-I MOSFIRE Spectroscopy of Compact Star-forming Galaxies at z >~ 2: High Velocity Dispersions in Progenitors of Compact Quiescent Galaxies. Astrophys J. 2014; 795:145.

29. van Dokkum P, et al. Forming Compact Massive Galaxies. Astrophys J. 2015; 813:23.
30. Postman M, et al. The Cluster Lensing and Supernova Survey with Hubble: An Overview. Astrophys J Suppl. 2012; 553:668.
31. Zitrin A, et al. The Cluster Lensing and Supernova Survey with Hubble (CLASH): Strong-lensing Analysis of A383 from 16-band HST/WFC3/ACS Imaging. Astrophys J. 2011; 742:117.
32. Zitrin A, et al. Hubble Space Telescope Combined Strong and Weak Lensing Analysis of the CLASH Sample: Mass and Magnification Models and Systematic Uncertainties. Astrophys J. 2015; 801:44.
33. Monna, A; , et al. Precise strong lensing mass profile of the CLASH cluster MACS 2129. 2016. Preprint at https://arxiv.org/abs/1605.08784
34. Geier S, et al. VLT/X-Shooter Near-infrared Spectroscopy and HST Imaging of Gravitationally Lensed z ~ 2 Compact Quiescent Galaxies. Astrophys J. 2013; 777:87.
35. Zabl J, et al. Deep rest-frame far-UV spectroscopy of the giant Lyman α emitter `Himiko'. Mon Not R Ast Soc. 2015; 451:2050.
36. Selsing J, et al. An X-Shooter composite of bright 1 < z < 2 quasars from UV to infrared. Astron Astrophys. 2016; 585:87.
37. Christensen L, et al. The low-mass end of the fundamental relation for gravitationally lensed star-forming galaxies at 1 < z < 6. Mon Not R Ast Soc. 2012; 427:1953–1982.
38. Jullo E, et al. A Bayesian approach to strong lensing modelling of galaxy clusters. New J Phys. 2007; 9:447–478.
39. Meneghetti M, et al. The Frontier Field Lens Modeling Comparison Project. arXiv1606.04548. 2016
40. Chabrier G. Galactic stellar and substellar initial mass function. Publ Astron Soc Pacif. 2003; 115:763–795.
41. Sandage A. Star formation rates, galaxy morphology, and the Hubble sequence. Astron Astrophys. 1986; 161:89–101.
42. Charlot S, Fall M. A Simple Model for the Absorption of Starlight by Dust in Galaxies. Astrophys J. 2000; 539:718–731.
43. Zibetti S, et al. Resolving the age bimodality of galaxy stellar populations on kpc scales. Mon Not R Ast Soc. 2017:252.
44. Valdes F, et al. The Indo-US Library of Coudé Feed Stellar Spectra. Astrophys J Supp. 2004; 152:251–259.
45. Wu Y, et al. Coudé-feed stellar spectral library – atmospheric parameters. Astron Astrophys. 2011; 525:A71.
46. Prescott M, Martin CL, Dey A. Spatially Resolved Gas Kinematics within a Lyα Nebula: Evidence for Large-scale Rotation. Astrophys J. 2015; 799:62.
47. Zibetti S. Introducing ADAPTSMOOTH, a new code for the adaptive smoothing of astronomical images. arXiv: 0911.4956. 2009
48. Zibetti S, et al. Resolved Stellar Mass Maps of Galaxies – I. Method and implication for Global Mass Estimates. Mon Not R Ast Soc. 2009; 400:1181–1198.
49. Peng CY, et al. Detailed Structural Decomposition of Galaxy Images. Astron J. 2002; 124:266–293.
50. Sarzi M, et al. The SAURON project - V. Integral-field emission-line kinematics of 48 elliptical and lenticular galaxies. Mon Not R Ast Soc. 2006; 366:1151–1200.
51. Müller-Sánchez F, et al. Outflows from Active Galactic Nuclei: Kinematics of the Narrow-line and Coronal-line Regions in Seyfert Galaxies. Astrophys J. 2011; 739:69.
52. Comerford JM, Green JE. Offset Active Galactic Nuclei as Tracers of Galaxy Mergers and Supermassive Black Hole Growth. Astrophys J. 2014; 789:112.
53. Lotz J, et al. The effect of mass ratio on the morphology and time-scales of disc galaxy mergers. Mon Not R Ast Soc. 2010; 404:575–603.
54. Hopkins P, et al. How do Disks Survive Mergers? Astrophys j. 2009; 691:1168–1201.
55. Szomoru D, Franx M, van Dokkum P. Sizes and Surface Brightness Profiles of Quiescent Galaxies at z ~ 2. Astrophys J. 2012; 749:121.

Europe PMC Funders Author Manuscripts

56. McGrath E, et al. Morphologies and Color Gradients of Luminous Evolved Galaxies at z~ 1.5. Astrophys J. 2008; 682:303–318.
57. Stockton A, Canalizo G, Maihara T. A Disk Galaxy of Old Stars at z~2.5. Astrophys J. 2004; 605:37–44.
58. Hsu L-Y, Stockton A, Shin H-Y. Compact Quiescent Galaxies at Intermediate Redshifts. Astrophys J. 2014; 796:92.
59. Trujillo I, et al. NGC 1277: A Massive Compact Relic Galaxy in the Nearby Universe. Astrophys J. 2014; 780:20.
60. van der Wel A, et al. The Majority of Compact Massive Galaxies at z~2 are Disk Dominated. Astrophys J. 2011; 730:38.
61. Hill A, et al. A Stellar Velocity Dispersion for a Strongly-lensed, Intermediate-mass Quiescent Galaxy at z=2.8. Astrophys J. 2016; 819:74.
62. Magdis G, et al. The evolving Interstellar Medium of Star-Forming Galaxies since z=2 as Probed by Their Infrared Spectral Energy Distribution. Astrophys J. 2012; 760:6.
63. Coe D, et al. CLASH: Precise New Constraints on the Mass Profile of the Galaxy Cluster A2261. Astrophys J. 2012; 757:22.
64. Puech M, et al. 3D Spectroscopy with VLT/GIRAFFE. IV. Angular momentum and dynamic support of intermediate redshift galaxies. Astron Astrophys. 2007; 466:83–92.
65. Puech M, et al. IMAGES III. The evolution of the near-infrared Tully-Fisher relation over the last 6 Gyr. Astron Astrophys. 2008; 484:173–187.

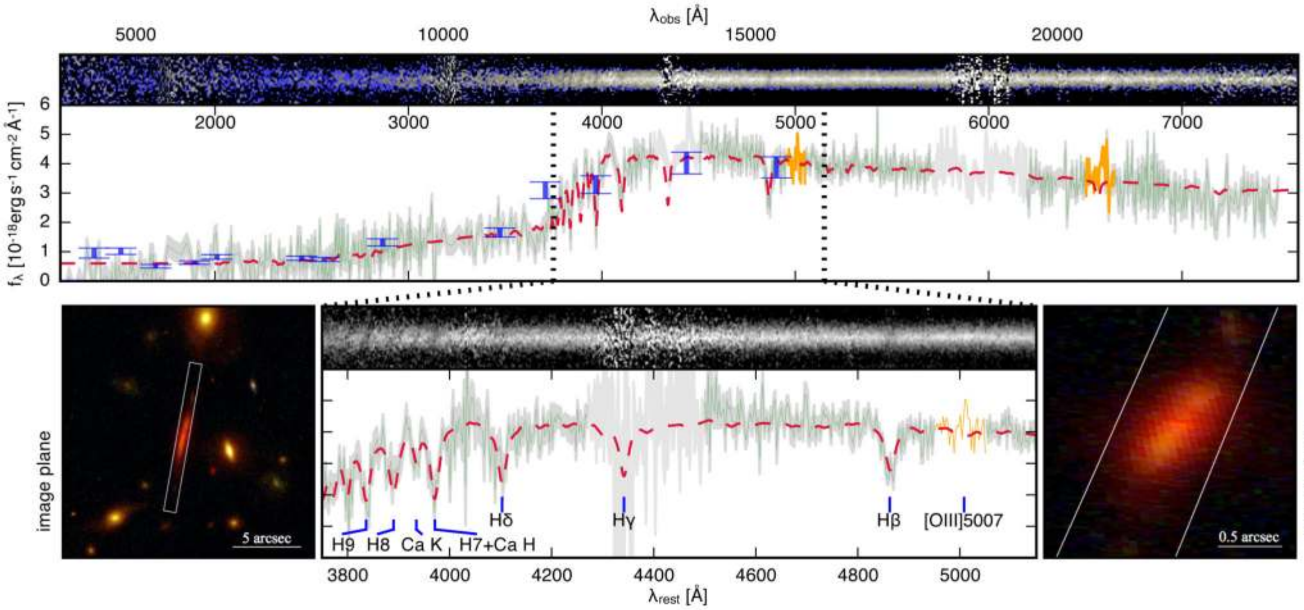

Figure 1.

Spectrum of MACS2129-1. Rest-frame UV-optical 2D and 1D XSHOOTER spectrum, adaptively rebinned to a constant S/N per bin, and a zoom in on the most important absorption features, binned to a resolution of 9.6Å (observed). The dashed red line shows the best-fit stellar population model. Grey/orange colored regions indicate windows of high telluric absorption/important emission lines. Also shown are color composite HST images on the image and reconstructed source plane, with the position of the slit overlaid.

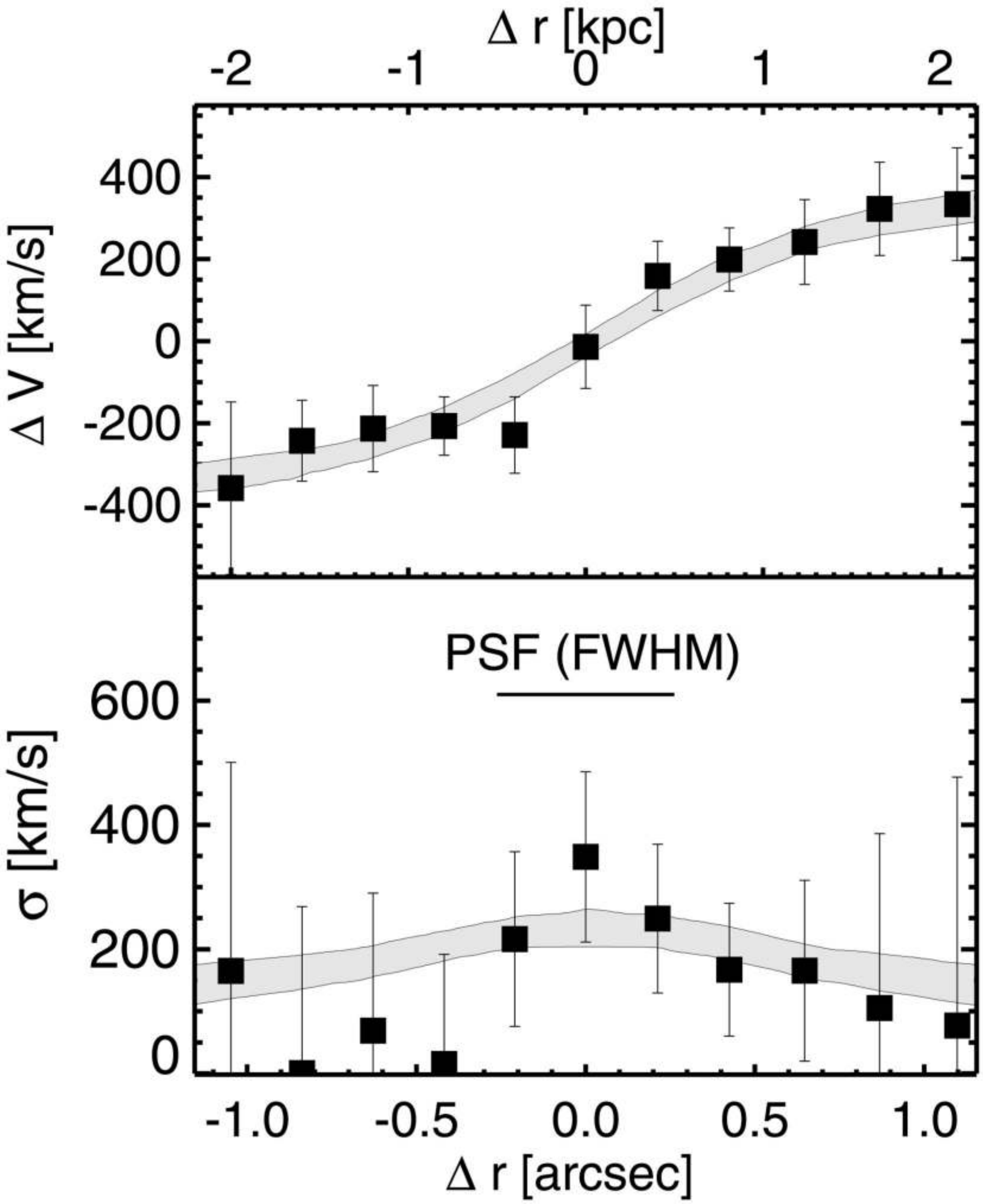

Figure 2.

Rotation and Dispersion curve for MACS2129-1. Velocity offsets and dispersions as a function of distance from the center of the galaxy, derived from pPXF fits to the individual spatial lines in the full spectrum. The grey polygon shows the best fitting thin disk model (**±1σ**) to the black squares. The observed dispersion is high in the center and drops off symmetrically with distance, consistent with the effect of PSF smearing of the velocity gradient, and a constant dispersion of up to ~100 km/s (grey polygon).

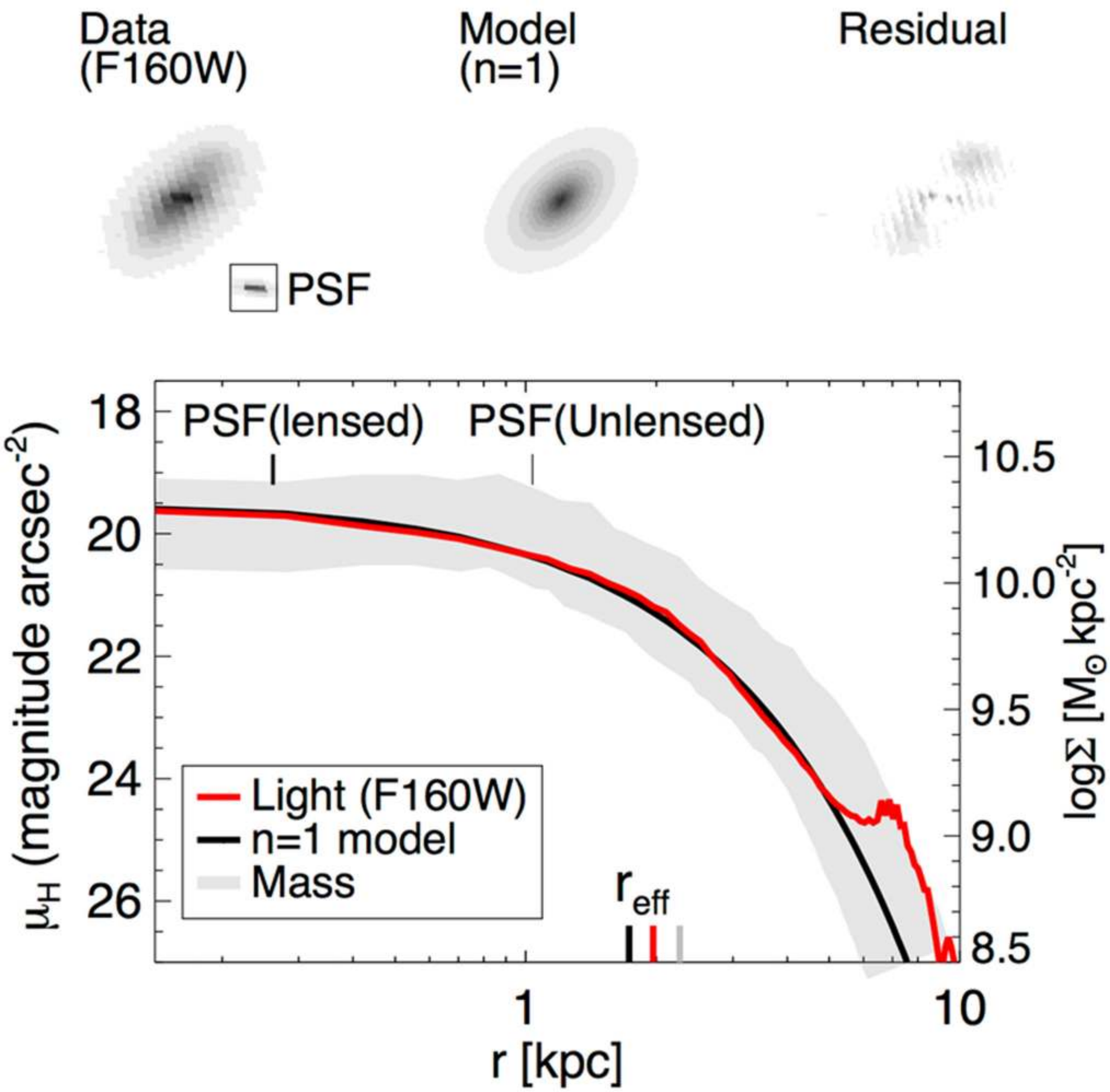

Figure 3.

Stellar population maps on the reconstructed source plane. These are created from fits to the HST imaging, using the same stellar population library, as used to fit the full spectrum. The insets show 68% confidence intervals for the derived parameters. The PSF is shown in Figure 4. The younger knot in the top right corner, which may be an ongoing minor merger does not give rise to the extra light seen in Figure 4, or influence the conclusions based on azimuthally averaged profiles (see Methods).

Europe PMC Funders Author Manuscripts

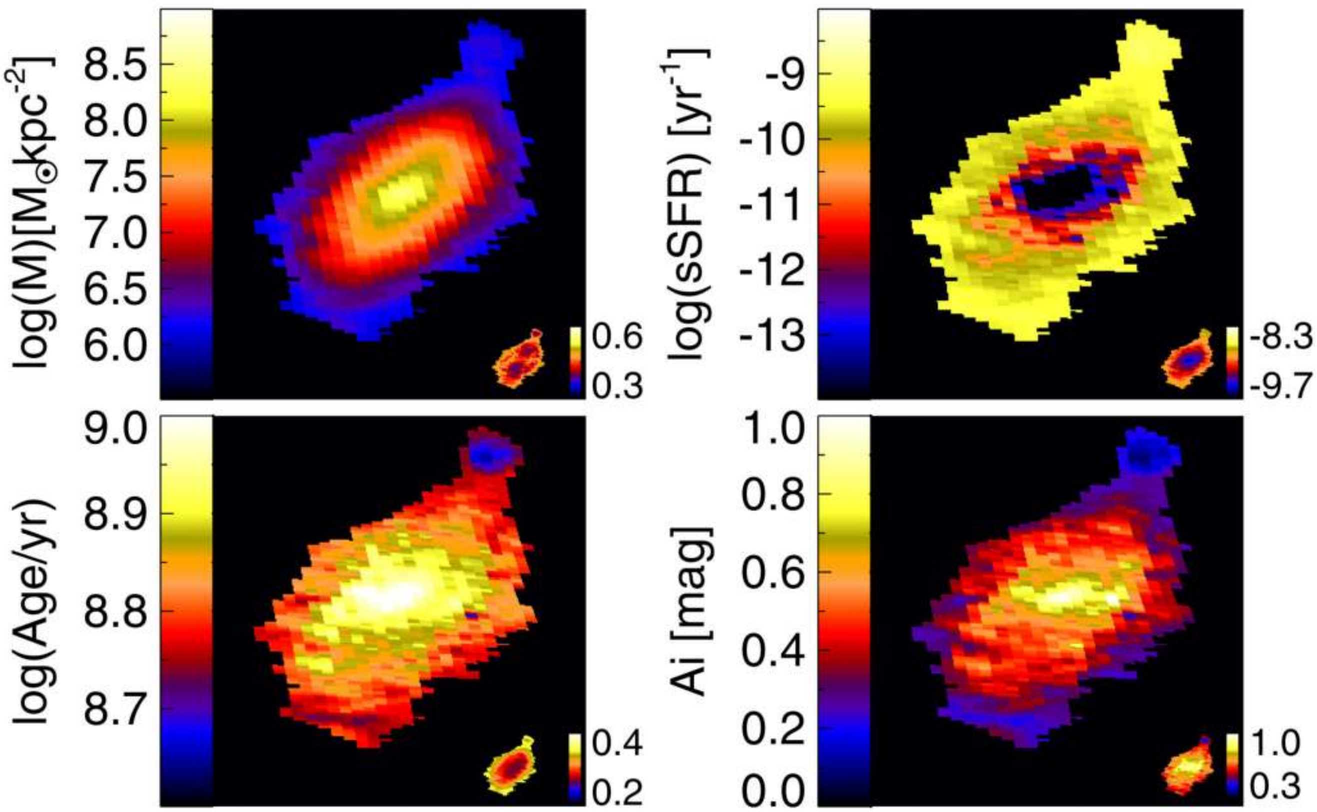

Figure 4.

Surface brightness and stellar mass profile for MACS2129-1. Left: Top panel shows the source plane reconstruction of WFC3/F160W band image with the PSF shown as an inset. Second panel shows the best fitting Sersic model ($n = 1.01^{+0.12}_{-0.06}$). Third panel shows the residual, which may show a hint of spiral structure. Right: The 1D light and surface mass density profiles (derived in elliptical apertures, following the best fitting Sersic model) are both well represented by an n=1 exponential disk model. The increased spatial resolution due to lensing is illustrated by the (circularized) HWHM of the PSF at z=2.15, with and without lensing.